Aeroelastic Control-oriented Modeling of an Air-breathing Hypersonic Vehicle

Praneeth Reddy Sudalagunta[*], Cornel Sultan[†], Rakesh K. Kapania[‡], Layne T. Watson[§], and Pradeep Raj [¶]

Virginia Tech, Blacksburg, VA, 24061, USA

Modeling aeroelastic effects for an air-breathing hypersonic vehicle is challenging due to its tightly integrated airframe and propulsion system that leads to significant deflections in the thrust vector caused by flexing of the airframe. These changes in the orientation of the thrust vector in turn introduce low frequency oscillations in the flight path angle, which make control system design a challenging task. The air-breathing hypersonic vehicle considered here is assumed to be a thin-walled structure, where deformations due to axial, bending, shear, and torsional loads are modeled using the six independent displacements of a rigid cross section. Complex interactions between the airframe and the associated hypersonic flow field may introduce lightly damped high frequency modes. Such high frequency free vibration modes are computed accurately using a novel scheme previously developed. The nonlinear equations of motion for the flexible aircraft are derived, these equations are then linearized about a computed cruise condition, and selective modal analysis is carried out on the linearized system. Further, a linear quadratic regulator (LQR) is designed to compensate for perturbations in initial conditions, where a novel and practical approach is used to populate the weighting matrices of the LQR objective function.

Nomenclature

A	State coefficient matrix
B	Control coefficient matrix
B_e	Linearized control coefficient matrix
$\mathbf{C}$	Coriolis and gyroscopic forces and moments vector
C_e	Linearized matrix accounting for damping and gyroscopic effects
D	Drag, N

[*]Postdoctoral Fellow, Moffitt Cancer Center and Research Institute, Tampa, FL, 33612
[†]Associate Professor, Aerospace & Ocean Engineering, Blacksburg, VA, 24061, Senior Member, AIAA
[‡]Mitchell Professor, Aerospace & Ocean Engineering, Blacksburg, VA, 24061, Associate Fellow, AIAA
[§]Professor, Computer Science, Mathematics, and Aerospace & Ocean Engineering, Blacksburg, VA, 24061
[¶]Professor, Aerospace & Ocean Engineering, Blacksburg, VA, 24061, Fellow, AIAA

$\mathbf{d_E}$ Vector of instantaneous deformations
$\mathcal{J}$ Cost functional
K Optimal feedback constant
K_e Linearized stiffness matrix
L Lift, N
$\mathcal{L}$ Lagrangian
L_f Length of the forebody, m
L_n Length of the nacelle, m
L_a Length of the aftbody, m
M_e Linearized mass matrix
$M_{\mathcal{T}}$ Moment due to thrust, N-m
$\mathcal{M}$ Mass matrix
m Vehicle mass, kg
$\mathbf{K}$ Conservative forces and moments vector
$\mathbf{p}$ Position vector of a point P on the airframe with respect to vehicle fixed frame, V
$\mathbf{p}'$ Position vector of a point P on the airframe with respect to the inertial frame, I
$\mathbf{p}_v$ Position vector of vehicle fixed frame, V
$\mathbf{Q}_{\mathrm{a}}$ Aerodynamic force vector
$\mathbf{Q}_{\mathrm{u}}$ Control forces and moments vector
$\mathbf{q}$ Vector of generalized coordinates
R Rotation matrix from V frame to I frame
T Kinetic energy, J
$\mathcal{T}$ Thrust, N
t Time, s
$\mathbf{u}_{cs}$ Vector of control surface deflections
$\bar{u}_i$ Displacement of the cross section along x_i
V Elastic strain energy stored in the structure, J
W Vehicle weight, N
$\mathbf{x}$ State variable vector
x_1 Independent spatial coordinate along the longitudinal axis, m
x_2 Independent spatial coordinate along the lateral axis, m
x_3 Independent spatial coordinate perpendicular to the lateral and longitudinal axes, m
α Angle of attack
δ Perturbed generalized coordinate
$\boldsymbol{\eta}$ Vector of modal coordinates
λ Lame's first parameter, G Pa
μ Lame's second parameter or shear modulus, G Pa
Ω Diagonal matrix with free vibration natural frequencies
ϕ Mode shape function
$\boldsymbol{\theta}_{V,I}$ Vector of Euler angles describing the orientation of the vehicle fixed frame
ρ Material density, kg/m^3
ω Natural frequency, rad/s

Subscript

$i = 1, 2, 3$ Forces along x_i axis
$j = 4, 5, 6$ Moments along x_j axis
cg Center of gravity

eq Equilibrium condition

I. Introduction

Air-breathing hypersonic vehicle (AHV) technology finds potential applications in single stage to orbit (SSTO)/two stage to orbit (TSTO) space missions and long range cruise missions. The advancement in aircraft structures and propulsion technology has fueled interest in developing a full scale air-breathing hypersonic vehicle. Although AHVs offer attractive benefits such as making low-earth orbit space missions reliable and affordable [1], long range cruise missions cheaper [2], high speed commercial air travel possible [3], etc., they pose myriad technological challenges in the form of aerothermoelastic effects [4], integrated airframe and propulsion system [5], and nonminimum phase behavior [6].

An air-breathing hypersonic vehicle is a long, slender lifting body with a sharp leading edge for drag reduction [7]. Such an aircraft would experience aerodynamic heating at the stagnation point, in the nacelle region close to the combustion chamber, and along the aft body panel housing the exhaust nozzle [5]. This would influence the associated flow field over the aircraft and material properties of the structure. Coupling between the unsteady aerodynamics, thermodynamics, and structural dynamics will result in aerothermoelastic effects. Studying such effects requires a trade-off between using simplified analytical methods against obtaining reduced order models from high fidelity computational tools [8].

The design vision for a hypersonic vehicle dates back to the end of World War I, supported by the works of Konstantin Tsiolkovsky, Robert H. Goddard, and Werner von Braun [9]. It wasn't until the late 1930s that these ideas were put to practice through experimental work. The first experiments were attributed to the development of a pre-World War II German A-series winged aircraft housing a V-2 rocket capable of reaching speeds beyond Mach 4 [10]. The modern day air-breathing hypersonic vehicle wasn't conceptualized until the early 1960s, fueled by the success of some of the early X-series aircraft developed in the United States of America [11]. The subsequent years would see the hypersonic vehicle's flight envelope extended up to Mach 14 through a joint U.S. Air Force and NASA program called ASSET (Aerothermodynamic/elastic Structural Systems Environmental Tests). These flight tests were carried out on aircraft with a waverider configuration, however, the propulsion system was still rocket based [12]. The hypersonic vehicle concept evolved into using a supersonic scramjet engine, as opposed to the conventional rocket propulsion, giving significant fuel savings and weight reduction by completely losing the oxidizer [13]. The projected performance benefits included a significant increase in range and endurance, reduction in fuel consumed, making the aircraft reusable, potential to land and take-off like conventional aircraft, reduction in time spent on preflight preparations, etc [14]. The benefits of using a scramjet engine were compelling, but came with a fair share of challenges. The only viable location for the scramjet engine was in the underbelly of the aircraft, resulting in a tightly integrated airframe and propulsion system. Moreover, the inflow into the engine was influenced by the forebody flexing, effectively coupling the aerodynamics, structural dynamics, and propulsion system [15]. Efforts to design a blended body aircraft encapsulating the nacelle of the scramjet engine began in the early 1970s and extended until the early 1980s [16]. Another joint U.S. Air Force and NASA program called NASP (National Aero-Space Plane) was initiated in the late 1980s to design a single stage to orbit air breathing hypersonic vehicle capable of

reaching speeds as high as Mach 25 [17]. Such a vehicle would have to fly at lower altitudes to achieve reasonable hypersonic propulsive efficiency leading to extreme aerothermal loads and adverse temperature gradients [18]. This period saw the emergence of several mathematical models that dealt with varying levels of complexity in order to model the dynamics of a single stage to orbit hypersonic reentry vehicle [19]. The aeropropulsive models developed under this program were later used in the Hyper-X program by NASA. The mission statement of this initiative was to incrementally achieve technological progress, as opposed to developing a full-scale vehicle. Further, the cruise speed decreased from Mach 25 to Mach 5–10 and the single stage to orbit vehicle was revised to a two stage to orbit vehicle [20]. The prototypical Hyper-X demonstrator vehicle was 12 feet long and was envisioned to be scaled to a 200 foot long full-scale aircraft [21]. The focus of this period was to tackle several control challenges that seemed too far fetched earlier. Subsequent efforts in this area were made in developing the two stage to orbit reusable launch vehicle for low earth orbit space missions by NASA as part of the Hyper-X program, and a long range high altitude hypersonic cruise vehicle by the U.S. Air Force as part of the HyTech program [16].

The available literature of interest pertaining to the design of AHVs can be broadly classified into three mutually exclusive groups: studies on aerothermoelastic effects, vehicle dynamics modeling, and control system design.

A. Aerothermoelastic Studies

Studies on aerothermoelastic effects date back to the early 1960s. As the focus shifted towards scramjet propulsion, the nature of these effects changed drastically requiring a complete revamp of the aerothermoelastic modeling efforts. Recent efforts by McNamara and Friedman [7, 8] explored the effects of coupling between unsteady hypersonic aerodynamics and thermodynamics on the structure. Klock et al. [4] carried out simulations of the aerothermoelastic effects on the longitudinal dynamics of the flexible aircraft. Culler, Williams, and Bolender [22] extended the nonlinear longitudinal dynamics model by Bolender and Doman [5] to account for the effects of varying mass and average temperature along the trajectory. Notable studies on the effect of aerothermoelasticity on control surface panels for flutter analysis include those by Chao et al. [23], Abbas et al. [24], and Falkiewicz et al. [25]. Although each of these works contribute to a growing body of literature in their own way and provide valuable insight, they are not high fidelity control design worthy models.

B. Vehicle Dynamics Modeling

Most of the hypersonic vehicle dynamics models developed in the past two decades are restricted to nonlinear ODE models describing the aircraft's behavior along the longitudinal direction. Early efforts by Chavez and Schmidt [19] account for flexibility effects in the transverse direction and modeled aeropropulsive effects for the first time. Seminal works by Bolender and Doman [5, 26] extended this work by advancing the aerodynamics model from Newtonian impact theory to oblique shock theory to including viscous effects. Torrez et al. [27] furthered this work by improving the propulsion system modeling through a dual mode scramjet engine. The focus then shifted to control-oriented modeling, where the modeling focus is to facilitate implementation of efficient control laws [2, 28–31]. The

aforementioned works consistently focus on studying the longitudinal dynamics of the vehicle. The only work that studies the impact of longitudinal and lateral-directional dynamics is by Keshmiri [32]. However, this work only addresses low-fidelity flexibility effects. All efforts unanimously ignore high frequency effects, assuming them to be easily damped out. A major contribution of our work is to acknowledge that this assumption needs to be verified by modeling and studying the effects of these high frequency modes.

C. Control System Design

The Hyper-X program's test flights shed some light on the impending control challenges to be tackled in making hypersonic air-breathing flight a reality. Over the past two decades, control system design efforts for an air-breathing hypersonic vehicle range from treating the airframe as a rigid body, to modest introduction of the airframe's coupling effects, using a linearized hypersonic aerodynamics model, etc. Works by Fiorentini et al. [6, 33, 34] focus on the nonminimum phase behavior of the aircraft, and propose to use nonlinear control techniques to compensate for such behavior. Sigthorsson et al. [35, 36] use robust linear and nonlinear control techniques by taking only the first three fundamental modes of vibration into consideration. A control-oriented model developed by Parker et al. [37] shows control laws that work for low fidelity structural models don't necessarily work for high fidelity ones, thus emphasizing the need for greater fidelity in the control models in order to develop realistic control laws.

The body of literature developed so far, despite being diverse, leaves some voids, like studying the effect of high frequency modes on the dynamics, modeling lateral-directional dynamics, implementing high fidelity structural modeling accounting for shear effects, etc. Therefore, there is a growing need for a comprehensive approach with a computationally tractable, high fidelity model. Bolender [26] lists nine subject areas pertaining to AHV modeling that need to be addressed. Two of the nine subject areas were isolated to be addressed in this paper, namely, the capability for 6DOF simulations using a 3D aerodynamic model, and the development of accurate first principles based models that do not require CFD and FEM analysis to be run apriori.

In this work an air-breathing hypersonic vehicle is characterized by an airframe tightly integrated with a scramjet propulsion system. The aerodynamic loads cause relatively large deformations of the forebody that affect the air flow into the inlet, causing significant changes in both magnitude and orientation of the resulting thrust vector. The airframe is modeled as a thin-walled structure assuming that a plane section remains plane and not necessarily perpendicular to its instantaneous axis taking into account axial, bending, shear, and torsional effects. None of the control-oriented models presented in the available literature account for such high fidelity flexibility effects, making this approach unique and its impact significant. Such a treatment also allows for the lateral-directional dynamics to be modeled, and its interaction with the longitudinal dynamics to be studied. Six independent displacements of a rigid cross section are used to describe the deformation at a given point on the vehicle making the free vibration problem one-dimensional. The deformation at a given point on the vehicle is expressed as a superposition of the first n significant modes, where each mode is expressed as the product of a mode shape function $\phi(x)$ and a modal coordinate $\eta(t)$. The free vibration problem is solved to compute the mode shapes for the first n significant

modes, using the Ritz method to estimate natural frequencies for the first n modes as initial guesses for a two-point boundary value problem solver SUPORE [38], which solves the governing equations subject to appropriate boundary conditions to accurately compute the mode shapes of the vehicle [39]. The first 14 free vibration modes are used to study the flexibility effects of an AHV by deriving a system of nonlinear equations of motion. These equations are derived using the principle of virtual work, where the virtual work due to applied (aerodynamic, gravitational, and control) forces is equated to the virtual work due to internal forces (inertial effects and elastic forces) using the Lagrangian approach. These form the nonlinear second order equations of motion for the flexible air-breathing hypersonic vehicle taking into account the interaction between aerodynamic, gravitational, control, inertial, and vibrational effects. Free vibration analysis of the vehicle's geometry reveals that the axial and transverse modes, and lateral and torsional modes, are coupled [40]. The proposed vehicle dynamics model accounts for flexibility effects due to the first ten axial-transverse modes and the first four lateral-torsional modes. Studying the effects of lateral vibration and torsion in a control-oriented paradigm is a first for this class of vehicles. Further, the nonlinear equations of motion are linearized about a given cruise condition to obtain the linearized dynamics model. The first order linearized system's stability about the cruise condition is analyzed and the effect of unstable modes on the state variables is studied. The primary objective of this work is to study the effect of high frequency modes on the stability and performance of an air-breathing hypersonic vehicle. In order to stabilize the aircraft, a linear quadratic regulator (LQR) is proposed. The normalized weighting matrices for the objective function are expressed as a function of four independent parameters. Parametric analysis is conducted to find a set of parameters that maximize the stability margin. The closed-loop eigenvalues are presented for the most stable configuration resulting from a novel parametrization.

II. Problem Description

The nonlinear equations of motion for a flexible AHV integrate a structural dynamics model, an aeropropulsive model, and an actuator model for the control surfaces using the principle of virtual work. Inertial and vibrational interactions are considered internal to the structure, while aerodynamic, gravitational, and control forces are considered external.

A. Structural Dynamics Model

The airframe is modeled as a thin-walled structure, where six independent displacements of a rigid cross section define the deformation at a given point allowing for axial, bending, shear, and torsional effects. Figure 1 presents a three sided view of the airframe geometry. The upper fore body panel, shown in the side view, extends the entire length of the aircraft with an angle of inclination τ_{1u} with respect to the longitudinal axis, while the lower fore body panel spans the length of the fore body L_f and makes an angle τ_{1l} with the axis. The panel of the lower nacelle region is parallel to the axis and has a length L_n. The lower aft body panel that forms a part of the exhaust nozzle stretches through the length of the aft body L_a and makes an angle τ_2 with the upper fore body panel. The upper panel, shown in the top view, is modeled as an isosceles trapezoid with a height equal to the length of the aircraft L, and base lengths equal to the width of the aircraft at the fore body tip and the

aft body tip. This view also shows the location of the rudders and elevons located aft of the aircraft. The cross section, shown in Fig. 1, is modeled as a rectangle above the longitudinal

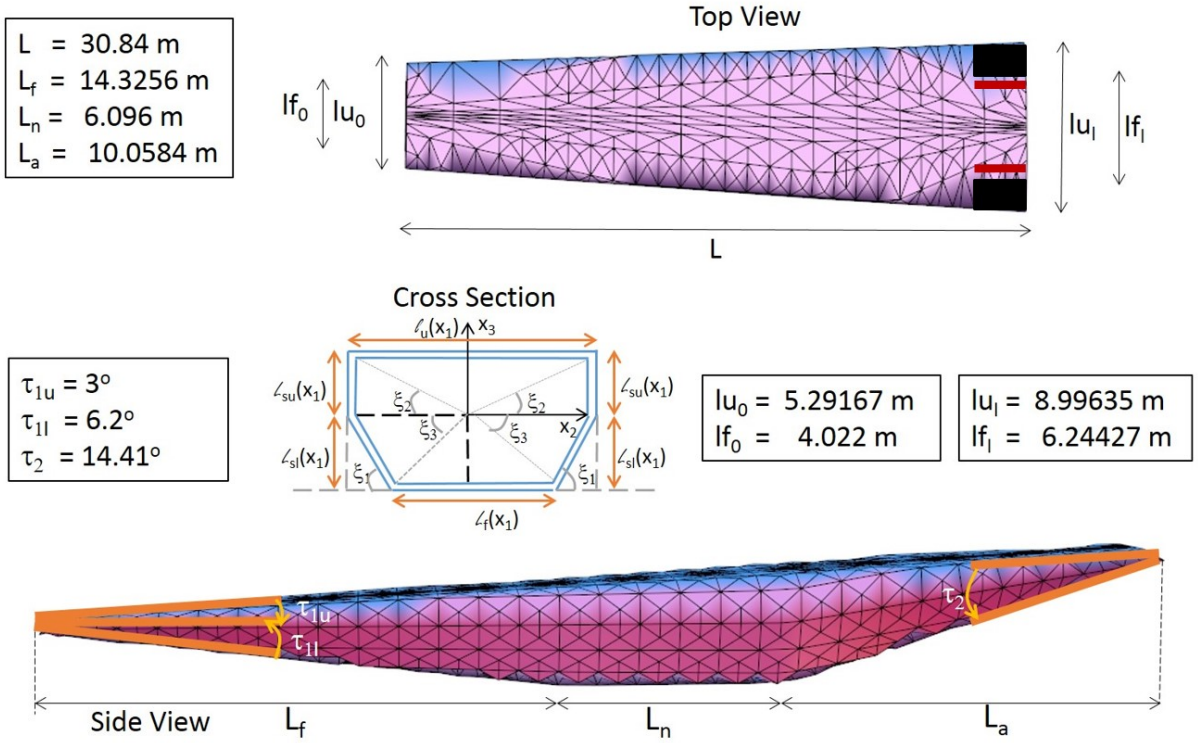

Figure 1: Three sided view of a typical air-breathing hypersonic vehicle (Figures not to scale)

axis and as an isosceles trapezium below. The trapezoidal lower cross section derives from the requirement that a fore body compression ramp needs to be flat in the lateral direction as opposed to being curved. A curved lower cross section would create a shear layer across the compression ramp (laterally) leading to nonuniform flow at the engine inlet. The length of the rectangular section l_u is the width of the upper panel, while l_f, the base of the trapezoidal section, is the width of the lower panel of the aircraft. The height of the rectangular section l_{su} and that of the trapezoidal section l_{sl} are heights of the upper and lower side panels of the aircraft. The cross section from Fig. 1 is defined by

$$l_{su}(x_1) = \begin{cases} x_1 \tan\tau_{1u}, & 0 \le x_1 \le L_f + L_n, \\ (L - x_1)\left(\frac{L_f + L_n}{L_a}\right)\tan\tau_{1u}, & L_f + L_n \le x_1 \le L, \end{cases} \tag{1}$$

$$l_{sl}(x_1) = \begin{cases} x_1 \tan\tau_{1l}, & 0 \le x_1 \le L_f, \\ L_f \tan\tau_{1l}, & L_f \le x_1 \le L_f + L_n, \\ (L - x_1)\left(\tan(\tau_2 + \tau_{1u}) - \frac{L}{L_a}\tan\tau_{1u}\right), & L_f + L_n \le x_1 \le L, \end{cases} \tag{2}$$

$$l_u(x_1) = l_{u0} + 2x_1 \tan\zeta_u, \tag{3}$$

$$l_f(x_1) = l_{f0} + 2x_1 \tan\zeta_f. \tag{4}$$

Nonstructural mass of the aircraft is modeled as a rigid circular disc circumscribed by the

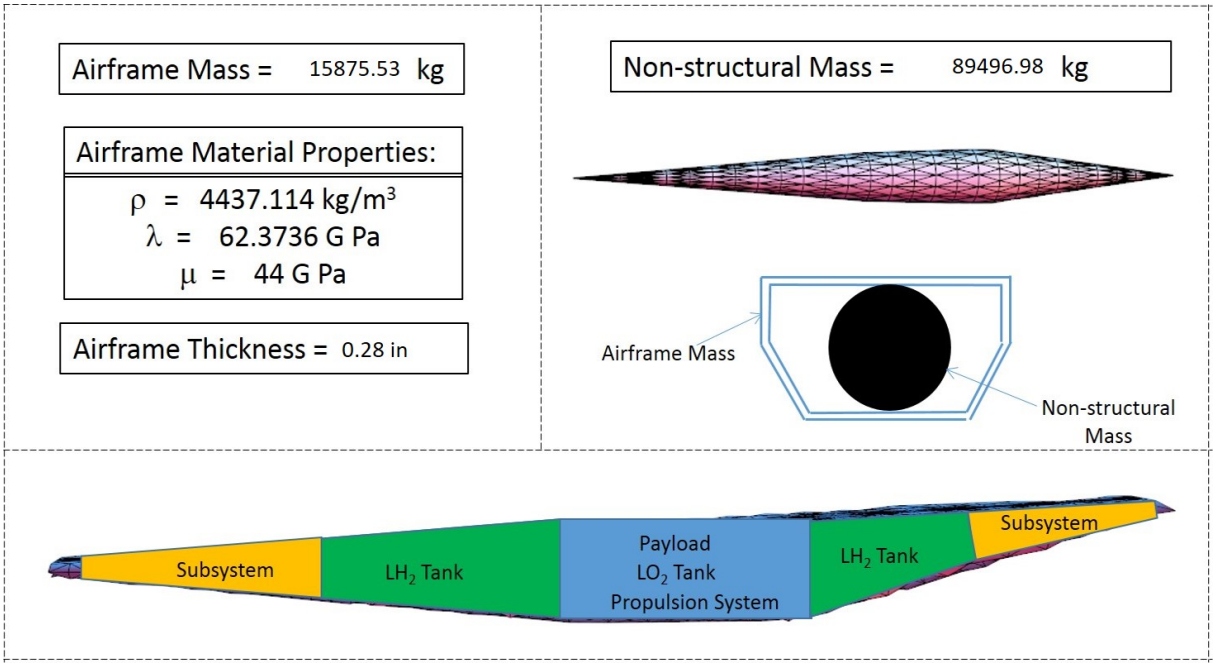

Figure 2: Nonstructural mass distribution

cross section as shown in Fig. 2. The disc density depends on the weight of each of the non-structural elements considered. For a detailed description of the distribution of nonstructural mass and computation of free vibration mode shapes, see Ref. [38].

B. Aeropropulsive Model

The airframe is assumed to have a long, wedge shaped fore body and a sharp leading edge that creates at the tip of the aircraft an oblique shock, which is almost entirely swallowed by the engine inlet [5]. The lower fore body panel acts as a compression ramp for the scramjet engine housed in the under belly of the nacelle region. The aft body is also wedge shaped where its lower panel forms a part of the exhaust nozzle for the engine along which a shear layer is created between the exhaust gases and the adjacent free stream. Aerodynamic panel pressures are computed using the models described in Fig. 3. The aeropropulsive model in the logitudinal direction is inherited from the literature [5]. Aerodynamic pressures on the side panels are computed using Newtonian impact theory. Based on its mission profile an AHV would have to be trimmed at a wide range of altitudes. The following atmospheric model estimates freestream conditions for altitudes ranging from $85,000$ ft to $110,000$ ft [41].

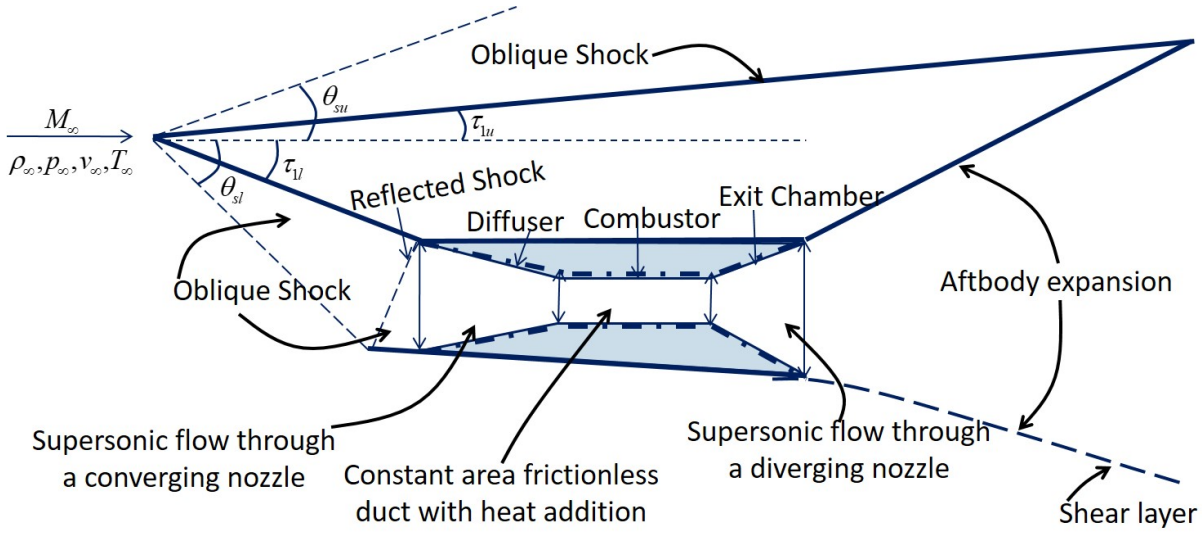

Figure 3: Longitudinal aeropropulsive model

The freestream temperature, pressure, and density at a given altitude are

$$T_\infty = T_0 \left(1 + K_0 \left(\frac{h_g - h_0}{T_0}\right)\right), \tag{5}$$

$$p_\infty = p_0 \left(1 + K_0 \left(\frac{h_g - h_0}{T_0}\right)\right)^{-g/(K_0 R)}, \tag{6}$$

$$\rho_\infty = \rho_0 \left(1 + K_0 \left(\frac{h_g - h_0}{T_0}\right)\right)^{-g/(K_0 R)-1}, \tag{7}$$

where the geopotential altitiude is

$$h_g = \frac{h R_e}{h + R_e}, \tag{8}$$

g is the acceleration due to gravity, R_e is the radius of the earth, and R is the specific gas constant. For a detailed derivation of the aerodynamic pressure distributions and thrust, see Ref. [42].

Table 1: Table of constants for the atmospheric model.

Alt Range (k ft)	Base Alt, h_0 (ft)	p_0 (lb-f/ft^2)	T_0 (°R)	ρ_0 (slug/ft^3)	K_0 (°R/ft)
65 − 104	104986.878	114.343	389.97	0.0001708	0.00054864
104 − 154	154199.475	18.12831	411.57	2.566003×10^{-5}	-0.00356616

C. Actuator Model

The air-breathing hypersonic vehicle has four control surfaces: two elevons and two rudders located aft of the aircraft as shown in Fig. 4. Control surfaces are modeled as rigid flat plates, hinged at the mid-chord location and free to rotate about their axis. It is assumed that all the control surfaces are located wide enough on the fuselage so that the freestream hypersonic flow would be incident on the control surfaces, as opposed to a mixture of freestream and associated flow field over the airframe. Figure 5 shows a side view of the elevon with the

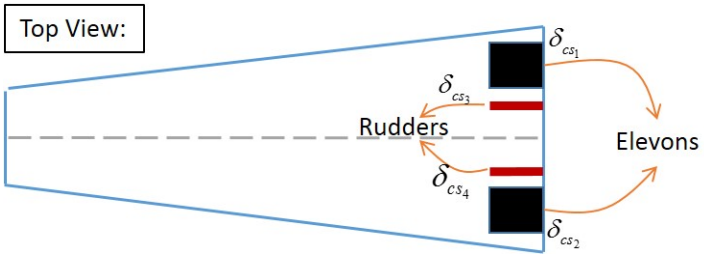

Figure 4: Top view showing the locations of the four control surfaces.

effect of the neutral axis bending captured through the angle

$$\theta_{def} = \left\{ \frac{\partial \phi_{\bar{u}_3}}{\partial x_1}\bigg| + x_2 \frac{\partial \phi_{\beta_1}}{\partial x_1} \right\}^T \boldsymbol{\eta}(t). \tag{9}$$

The blue line is the neutral axis and the black slab is the elevon, where α_0 is the angle of attack of the undeformed aircraft, M_∞ is the freestream Mach number, and δ_{cs} is elevon deflection about its mid chord point. The airframe's deformation reduces total available control surface deflection for implementing closed-loop control. When the angle of incidence

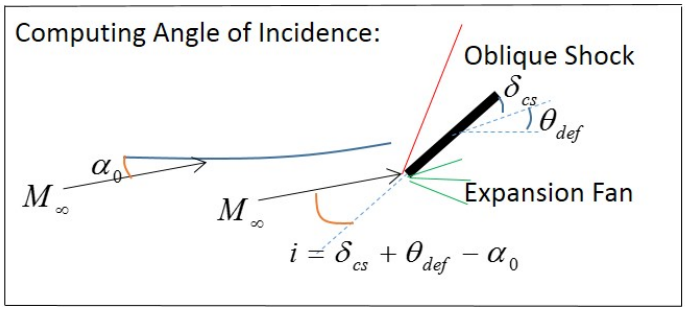

Figure 5: Side view of neutral axis and the elevon, showing the angle of incidence.

is greater than zero, the upper surface of the elevon experiences compression due to an oblique shock and the lower surface sees a Prandtl-Meyer expansion fan, as shown in Fig. 5. When the angle of incidence is less than zero, the upper surface experiences expansion and the lower surface experiences compression. Similarly, aerodynamic pressure distribution over the rudders is computed and all control forces are assumed to act on the respective hinged locations as point forces, see Ref. [42] for derivations.

III. Equations of Motion

A conventional aircraft modeled as a rigid body has six degrees of freedom in a six dimensional configuration space. A flexible aircraft, on the other hand, has infinitely many degrees of freedom in a infinite dimensional configuration space. Modal decomposition in a free vibration paradigm allows the first n significant modes to be used to describe flexibility effects, approximating the configuration space by a finite dimensional space. This is a key step in developing a control-oriented model, as it allows known control theoretic principles to be applied. Nonlinear equations of motion expressed in terms of a generalized coordinate vector uniquely describe the position of every point on the aircraft using six transport variables and n modal cordinates. There are three coordinate frames of interest, namely, the structural frame (fixed at the tip of the aircraft and aligned with the neutral axis of the undeformed body, used to compute free vibration mode shapes), the pseudo body frame (a floating frame of reference, fixed relative to the undeformed body), and the inertial ground frame (a non-accelerating frame of refernce, inertial with respect to the ground). Free vibration mode shape functions are computed in the structural frame, modal coordinates are expressed with respect to the pseudo body frame, and transport variables are measured with respect to the inertial ground frame. It would be convenient to choose the structural frame as the pseudo body frame to avoid transforming all the mode shape functions. Moreover, the surface of the earth is assumed to be flat and the effect of its rotation on the dynamics of the aircraft is neglected.

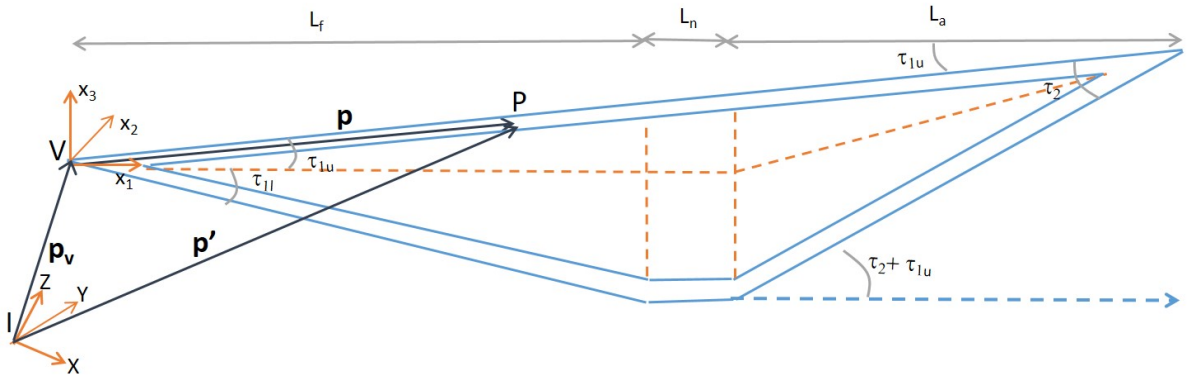

Figure 6: Location of vehicle frame and ground frame (Figure not to scale).

Figure 6 shows the location of the pseudo body frame, henceforth referred to as the vehicle frame V, relative to the inertial ground frame I, where the position and orientation of V with respect to I are given by the position vector $\mathbf{p}_v$ and the vector of 3-2-1 sequence Euler angles $\boldsymbol{\theta}_{V,I}$. The location of any point P on the aircraft with respect to I can be expressed in terms of $\mathbf{p}_v$, $\boldsymbol{\theta}_{V,I}$, and $\boldsymbol{\eta}$, the modal coordinates. The location of all points on the aircraft at a given instant of time determine the configuration of the vehicle and a generalized coordinate vector is composed of variables required to define this configuration.

The generalized coordinate vector $\mathbf{q}$ has size $6+n$ and is given by

$$\mathbf{q} = \left\{ \begin{array}{c} \mathbf{p}_v \\ \boldsymbol{\theta}_{V,I} \\ \boldsymbol{\eta} \end{array} \right\}. \tag{10}$$

Since $\mathbf{q}(t)$ describes the configuration of the vehicle for all time, the kinetic energy T of the vehicle is expressed in terms of $\dot{\mathbf{q}}$ and $\mathbf{q}$ by

$$T(\dot{\mathbf{q}},\, \mathbf{q}) = \frac{1}{2}\dot{\mathbf{q}}^T \mathcal{M}(\mathbf{q})\dot{\mathbf{q}}, \tag{11}$$

where

$$\mathcal{M}(\mathbf{q}) = \begin{pmatrix} m\,\mathbb{I}_{3\times 3} & (I_p + I_d(\boldsymbol{\eta}))_{3\times 3} & (I_\Phi)_{3\times n} \\ \left(I_p^T + I_d^T(\boldsymbol{\eta})\right)_{3\times 3} & \left(I_{pp} + I_{dd}(\boldsymbol{\eta}) + (I_{pd}(\boldsymbol{\eta}) + I_{pd}^T(\boldsymbol{\eta}))\right)_{3\times 3} & \left(I_{p\Phi} + I_{d\Phi}(\boldsymbol{\eta})\right)_{3\times n} \\ \left(I_\Phi^T\right)_{n\times 3} & \left(I_{p\Phi}^T + I_{d\Phi}^T(\boldsymbol{\eta})\right)_{n\times 3} & (I_{\Phi\Phi})_{n\times n} \end{pmatrix}, \tag{12}$$

$$I_p = \int_V \left(\mathbf{p}_{RB}{}^\times\right)^T \rho\, dV, \tag{13}$$

$$I_d = \int_V \left(\mathbf{d}_E{}^\times\right)^T \rho\, dV, \tag{14}$$

$$I_\Phi = \int_V \Phi\rho\, dV, \tag{15}$$

$$I_{pp} = \int_V \left(\mathbf{p}_{RB}{}^\times\right)^T \left(\mathbf{p}_{RB}{}^\times\right) \rho\, dV, \tag{16}$$

$$I_{dd} = \int_V \left(\mathbf{d}_E{}^\times\right)^T \left(\mathbf{d}_E{}^\times\right) \rho\, dV, \tag{17}$$

$$I_{pd} = \int_V \left(\mathbf{p}_{RB}{}^\times\right)^T \left(\mathbf{d}_E{}^\times\right) \rho\, dV, \tag{18}$$

$$I_{p\Phi} = \int_V \left(\mathbf{p}_{RB}{}^\times\right) \Phi\rho\, dV, \tag{19}$$

$$I_{d\Phi} = \int_V \left(\mathbf{d}_E{}^{\times}\right) \Phi \rho \, dV, \tag{20}$$

$$I_{\Phi\Phi} = \int_V \Phi^T \Phi \rho \, dV, \tag{21}$$

$\mathbb{I}_{3\times3}$ is a 3×3 identity matrix,

$$\left(\mathbf{y}^{\times}\right) = \begin{pmatrix} 0 & -y_3 & y_2 \\ y_3 & 0 & -y_1 \\ -y_2 & y_1 & 0 \end{pmatrix} \tag{22}$$

is a 3×3 skew symmetric matrix, $\mathbf{p_{RB}}$ is a position vector of a point on the undeformed aircraft,

$$\mathbf{d_E} = [\Phi(x_1, x_2, x_3)] \, \boldsymbol{\eta}(t) \tag{23}$$

is the vector of instantaneous deformations at a point, and $\Phi(x_1, x_2, x_3)$, or Φ is a matrix of mode shape functions (See Ref. [42] for a complete derivaton). The elastic strain energy U_e and the gravitational potential energy U_g of the vehicle are given by

$$U_e(\mathbf{q}) = \frac{1}{2} \boldsymbol{\eta}^T \left[\Omega^2 I_{\Phi\Phi}\right] \boldsymbol{\eta}, \tag{24}$$

$$U_g(\mathbf{q}) = -m\mathbf{g}^T \mathbf{p}_v - \mathbf{g}^T \mathbf{C}_{RB} - \mathbf{g}^T [I_\Phi] \boldsymbol{\eta}, \tag{25}$$

respectively, where Ω is an $n \times n$ diagonal matrix of natural frequencies for the first n significant modes obtained in Ref. [40], $\mathbf{C}_{RB}$ is the first moment of inertia of the undeformed aircraft, and $\mathbf{g}$ is the gravity vector in the inertial frame of reference. The Lagrangian is

$$\mathcal{L} = T(\dot{\mathbf{q}}, \, \mathbf{q}) - U_e(\mathbf{q}) - U_g(\mathbf{q}). \tag{26}$$

The nonlinear equations of motion for the flexible aircraft obtained using the Lagrangian are

$$\frac{d}{dt}\left(\frac{\partial \mathcal{L}}{\partial \dot{\mathbf{q}}}\right) - \frac{\partial \mathcal{L}}{\partial \mathbf{q}} = \mathbf{Q}_{\mathrm{a}} + \mathbf{Q}_u, \tag{27}$$

where $\mathbf{Q}_a$ and $\mathbf{Q}_u$ are the generalized forces due to aerodynamic and control forces and moments, respectively, derived from the virtual work due to these actions. The aerodynamics model inherited from Ref. [5] is used to compute the aerodynamic generalized forces and the thrust (See Ref. [40]). The generalized control forces vector is comprised of forces and moments due to the thrust and control surface deflections. The second order nonlinear equations of motion for a flexible aircraft obtained from Eq. (27) are

$$\mathcal{M}(\mathbf{q})\ddot{\mathbf{q}} + \mathbf{C}(\mathbf{q}, \, \dot{\mathbf{q}}) - \mathbf{Q}_{\mathrm{a}}(\mathbf{q}, \, \dot{\mathbf{q}}) + \mathbf{K}(\mathbf{q}) = \mathbf{Q}_u(\mathbf{q}, \, \dot{\mathbf{q}}, \, \mathbf{u}), \tag{28}$$

where $\mathbf{u}$ is the vector of control inputs, $\mathbf{C}(\mathbf{q}, \, \dot{\mathbf{q}})$ represents the Coriolis forces, $\mathbf{K}(\mathbf{q})$ represents forces due to the conservative force fields such as the gravitational potential energy and elastic strain energy. The effect of the airframe tightly integrated with the propulsion system

described earlier is modeled here through the angle of attack α, which depends on the structural deflection at the forebody tip of the aircraft, and to which the thrust is sensitive. Assuming that the AHV mission profile is predominantly cruise and that the vehicle does not turn into or away from the flow, the effect of shock induced transverse vibration dominates the longitudinal dynamics, which is modeled via the change in the angle of attack. Further, changes in the angle of attack affect the quality of the inflow into the engine inlet that influences the direction and magnitude of the thrust vector. Therefore, this model captures the effect of a flexible airframe on the thrust and through that the effect on the overall dynamics of the aircraft. It is important to note that $\alpha(t)$ is a function of $\boldsymbol{\eta}(t)$,

$$\alpha(t) = \alpha_0 + \left\{ \frac{\partial \phi_{\bar{u}_3}}{\partial x_1}\Big|_{x_1=0}^{T} \right\} \boldsymbol{\eta}(t), \tag{29}$$

and hence depends on $\mathbf{q}$.

IV. Equilibrium Conditions

A typical air-breathing hypersonic vehicle's mission profile is predominantly cruise. Hence, it would be appropriate to use this as the desired equilibrium configuration and design an appropriate closed-loop control system to ensure that the aircraft is stable while cruising. In this configuration, the aircraft does not accelerate, and hence attains dynamic equilibrium, which is characterized by zero net acceleration. The aircraft would be required to be trimmed at this desired cruise condition (no rotation) and it is assumed that it has structurally reached a steady state, with vibrations damped out. These conditions are expressed mathematically as

$$\begin{aligned} \ddot{\mathbf{q}}_{eq} &= \mathbf{0}, \\ \dot{\boldsymbol{\theta}}_{V,I_{eq}} &= \mathbf{0}, \\ \dot{\boldsymbol{\eta}}_{eq} &= \mathbf{0}. \end{aligned}$$

The above conditions are substituted into the nonlinear equations of motion, to obtain a set of $n+6$ nonlinear algebraic equations

$$\mathcal{M}(\mathbf{q})\ddot{\mathbf{q}} + \cancel{\mathbf{C}(\mathbf{q}, \dot{\mathbf{q}})} + \mathbf{K}(\mathbf{q}) = \mathbf{Q}_a(\mathbf{q}, \dot{\mathbf{q}}) + \mathbf{Q}_{cs}(\mathbf{q}, \dot{\mathbf{q}}, \mathbf{u}_{cs}, \mathrm{FER}) \tag{30}$$

in $n+14$ variables — three components of $\mathbf{p}_{v_{eq}}$, three components of $\dot{\mathbf{p}}_{v_{eq}}$, three Euler angles $\boldsymbol{\theta}_{V,I}$, fuel equivalence ratio FER, n modal coordinates $\boldsymbol{\eta}$, two elevon deflections (δ_{cs_1}, δ_{cs_2}), and two rudder deflections (δ_{cs_3}, δ_{cs_4}) as shown in Fig. 4. These four control surface deflections are populated in $\mathbf{u}_{cs}$.

The n modal coordinates $\boldsymbol{\eta}(t)$ are coupled to the transport variables dynamically. At equilibrium, the first six algebraic equations decouple from the remaining n equations. This simplifies the trim problem considerably. The n algebraic equations present a linear relationship between $\boldsymbol{\eta}(t)$ and aerodynamic panel pressures due to the assumption of linear elasticity of the structure.

$$\boldsymbol{\eta}_{eq} = \left[I_{\Phi\Phi}\Omega^2 \right]^{-1} \left\{ \mathbf{Q}_{a_{7-n}}(h, v_\infty, \mathrm{FER}) \right\}. \tag{31}$$

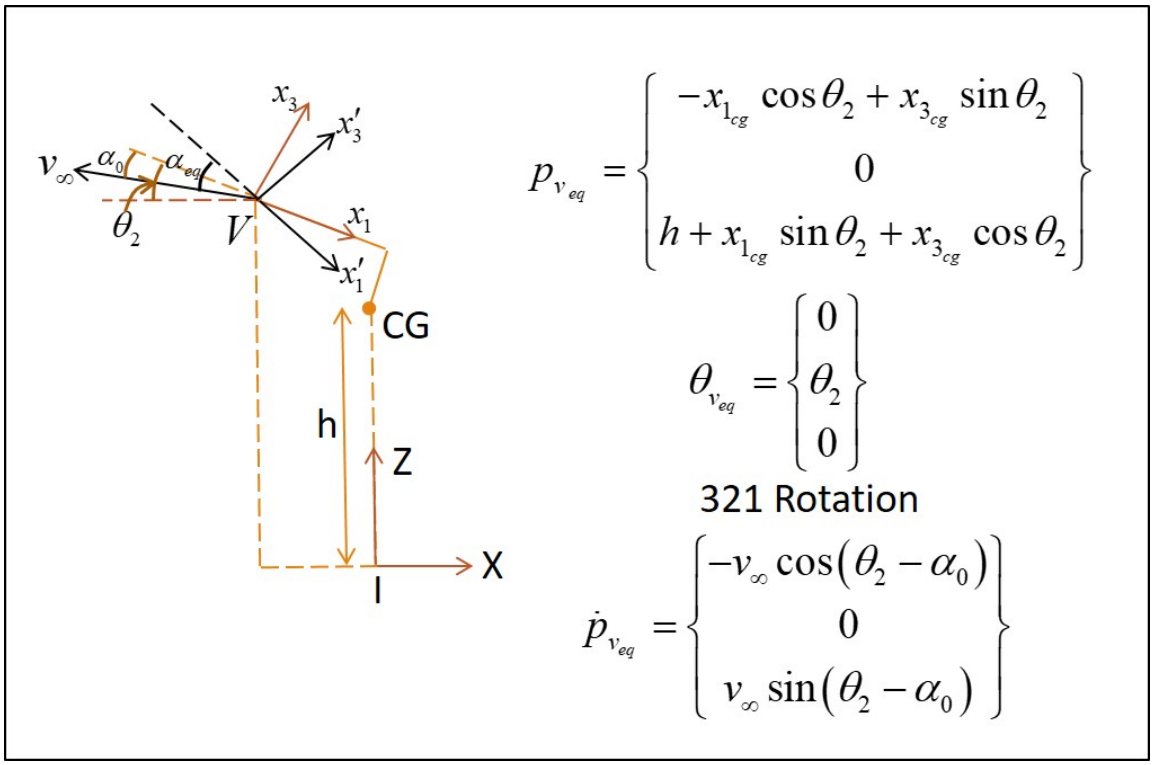

Figure 7: Simplifying assumptions at equilibrium.

This leaves six nonlinear algebraic equations in 14 variables. Carefully choosing the location and orientation of vehicle frame V as shown in Fig. 7 yields six equations in eight variables, namely, cruise altitiude h_{eq}, cruise velocity v_∞, pitch angle θ_2, aeroelastic angle of attack α_{eq}, and four control surface deflections in $\mathbf{u_{cs}}$. There are two angles of attack for this vehicle due to its flexible nature, namely, aeroelastic angle of attack α_{eq} measured from the instantaneous body axes $x_1' - x_3'$, and inertial angle of attack measured from the undeformed body axes $x_1 - x_3$ (pseudo body frame V). The former is used in computing aerodynamic panel pressures over the aircaft, while the latter serves the purpose of resolving velocity vector components with respect to the inertial ground frame I. Equation (29) evaluated at the

equilibrium yields α_{eq}, and is used to compute α_0.

$$\begin{Bmatrix} 0 \\ 0 \\ W \\ P_4(h,\, v_\infty,\, \boldsymbol{\eta}_{eq}) \\ P_5(h,\, v_\infty,\, \boldsymbol{\eta}_{eq}) \\ P_6(h,\, v_\infty,\, \boldsymbol{\eta}_{eq}) \end{Bmatrix} = \begin{Bmatrix} D(h,\, v_\infty,\, \mathrm{FER})\cos\theta_2 + L(h,\, v_\infty,\, \mathrm{FER})\sin\theta_2 \\ 0 \\ L(h,\, v_\infty,\, \mathrm{FER})\cos\theta_2 - D(h,\, v_\infty,\, \mathrm{FER})\sin\theta_2 \\ Q_{a_4}(h,\, v_\infty,\, \mathrm{FER}) \\ Q_{a_5}(h,\, v_\infty,\, \mathrm{FER}) \\ Q_{a_6}(h,\, v_\infty,\, \mathrm{FER}) \end{Bmatrix} + \begin{Bmatrix} -\mathcal{T}(h,\, v_\infty,\, \mathrm{FER})\cos\theta_2 \\ 0 \\ \mathcal{T}(h,\, v_\infty,\, \mathrm{FER})\sin\theta_2 \\ 0 \\ M_{\mathcal{T}}(h,\, v_\infty,\, \mathrm{FER}) \\ 0 \end{Bmatrix} + \begin{Bmatrix} Q_{cs_1}(h,\, v_\infty,\, \boldsymbol{\eta}_{eq},\, \mathbf{u}_{cs}) \\ Q_{cs_2}(h,\, v_\infty,\, \boldsymbol{\eta}_{eq},\, \mathbf{u}_{cs}) \\ Q_{cs_3}(h,\, v_\infty,\, \boldsymbol{\eta}_{eq},\, \mathbf{u}_{cs}) \\ Q_{cs_4}(h,\, v_\infty,\, \boldsymbol{\eta}_{eq},\, \mathbf{u}_{cs}) \\ Q_{cs_5}(h,\, v_\infty,\, \boldsymbol{\eta}_{eq},\, \mathbf{u}_{cs}) \\ Q_{cs_6}(h,\, v_\infty,\, \boldsymbol{\eta}_{eq},\, \mathbf{u}_{cs}) \end{Bmatrix}. \tag{32}$$

Symmetry about the $x_1 - x_3$ plane, and the assumpton that the aircraft doesn't turn into or away from the flow, leads to aerodynamic forces and moments canceling each other out in lateral-directional planes. By choosing the two rudder deflections δ_{cs_3} and δ_{cs_4} equal, the second, fourth, and sixth equations associated with side slip, roll, and yaw result in zero equations. From a mission design standpoint it would be desirable to choose cruise velocity and altitude, resulting in three equations and four varibles. A solution to this system was computed using a Lipschitzian-based search algorithm called DIRECT that minimizes the sum of squares of residuals for the three equations [43].

For a desired cruise altitude of 110, 000 ft and cruise Mach number of 10, the equilibrium conditions are

$$h_{eq} = 110,\, 000\,\mathrm{ft}, \qquad \alpha_{eq} = -0.43081527^\circ, \qquad M_{\infty_{eq}} = 10, \qquad \mathrm{FER}_{eq} = 0.93999677,$$
$$\delta_{cs_{1_{eq}}} = \delta_{cs_{2_{eq}}} = -4.5916^\circ, \qquad \delta_{cs_{3_{eq}}} = \delta_{cs_{4_{eq}}} = 2^\circ, \qquad \alpha_0 \approx \theta_2 = -0.0068572^\circ$$

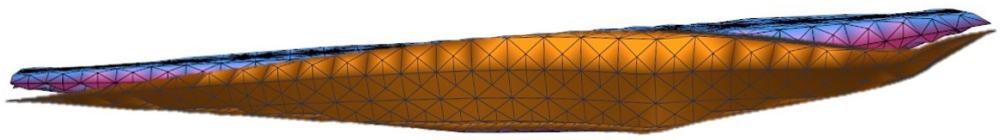

Figure 8: Side view of AHV's equilibrium configuration.

A side view of the deformed aircraft at equilibrium (in the foreground) with exaggerated deformations is presented in Fig. 8 and compared to the shape of the undeformed aircraft in

the background. Notice the change in the angle of attack at the front and the displacement of elevons at the back due to deformation.

V. Linearized Model

The primary performance expectation from a typical air-breathing hypersonic vehicle is to travel half way across the globe in about two hours, by consuming less than 50% of liquid hydrogen (LH_2) fuel available at take-off. Such extreme expectations are typical of high-speed, high-altitude, long range aircraft. This narrows down the mission profile to cruising at a very high altitude and a high Mach number, like the ones obtained in the previous section. At $110,000$ ft, due to highly rarefied atmosphere, the threat of high speed winds and gusts perturbing the aircraft from its equilibrium state is significantly lowered. The typical wind speeds above $100,\ 000$ ft are about $50-60$ knots, as found experimentally in Ref. [44]. The effect of gusts of magnitude $30-60$ m/s on the dynamics of an aircraft weighing $107,\ 000$ kg, traveling at speeds as large as 3000 m/s can be studied by linearizing the nonlinear equations of motion about the equilibrium conditions obtained earlier.

The nonlinear equations of motion derived earlier are

$$\mathcal{M}(\mathbf{q}(t))\ddot{\mathbf{q}}(t)+\mathbf{C}\left(\mathbf{q}(t),\dot{\mathbf{q}}(t)\right)+\mathbf{K}\left(\mathbf{q}(\mathbf{t})\right)=\mathbf{Q}_a\left(\mathbf{q}(t),\dot{\mathbf{q}}(t)\right)+\mathbf{Q}_c\left(\mathbf{q}(t),\dot{\mathbf{q}}(t),\mathbf{u}(t)\right), \tag{33}$$

where $\mathcal{M}(\mathbf{q}(t))$ is the matrix that represents the translational, rotational, and vibrational inertia of the aircraft, $\mathbf{C}\left(\mathbf{q}(t),\dot{\mathbf{q}}(t)\right)$ is a vector that represents Coriolis forces and gyroscopic moments, $\mathbf{K}\left(\mathbf{q}(\mathbf{t})\right)$ represents gravitational and elastic forces, $\mathbf{Q}_a\left(\mathbf{q}(t),\dot{\mathbf{q}}(t)\right)$ represents the aerodynamic forces, and $\mathbf{Q}_c\left(\mathbf{q}(t),\dot{\mathbf{q}}(t),\mathbf{u}(t)\right)$ represents the control forces. Equations (33) are linearized about a nominal solution $(\bar{\mathbf{q}},\ \dot{\bar{\mathbf{q}}})$ using small perturbation theory, where the state variables are expanded using a Taylor series approximation. By neglecting second order and higher order terms, a system of linear equations is obtained that represents the dynamics of the system of nonlinear Eqs. (33) accurately enough, provided the perturbations are small. The linearized equations of motion about an equilibrium flight are given by

$$M_e\,\ddot{\boldsymbol{\delta}}\mathbf{q}(t)+C_e\,\dot{\boldsymbol{\delta}}\mathbf{q}(t)+K_e\boldsymbol{\delta}\mathbf{q}(t)=B_e\boldsymbol{\delta}\mathbf{u}(t) \tag{34}$$

where

$$M_e=\mathcal{M}(\bar{\mathbf{q}}), \tag{35}$$
$$C_e=\nabla_{\dot{\mathbf{q}}}\mathbf{C}\left(\bar{\mathbf{q}},\dot{\bar{\mathbf{q}}}\right)-\nabla_{\dot{\mathbf{q}}}\mathbf{Q}_a\left(\bar{\mathbf{q}},\dot{\bar{\mathbf{q}}}\right)-\nabla_{\dot{\mathbf{q}}}\mathbf{Q}_c\left(\bar{\mathbf{q}},\dot{\bar{\mathbf{q}}},\bar{\mathbf{u}}\right), \tag{36}$$
$$K_e=\nabla_{\mathbf{q}}\mathbf{K}\left(\bar{\mathbf{q}}\right)+\nabla_{\mathbf{q}}\mathbf{C}\left(\bar{\mathbf{q}},\dot{\bar{\mathbf{q}}}\right)-\nabla_{\mathbf{q}}\mathbf{Q}_a\left(\bar{\mathbf{q}},\dot{\bar{\mathbf{q}}}\right)-\nabla_{\mathbf{q}}\mathbf{Q}_c\left(\bar{\mathbf{q}},\dot{\bar{\mathbf{q}}},\bar{\mathbf{u}}\right), \tag{37}$$
$$B_e=\nabla_{\mathbf{u}}\mathbf{Q}_c\left(\bar{\mathbf{q}},\dot{\bar{\mathbf{q}}},\bar{\mathbf{u}}\right). \tag{38}$$

A typical first-order dynamical system is given by

$$\dot{\mathbf{x}}(t)=A\mathbf{x}(t)+B\mathbf{u}(t). \tag{39}$$

Equation. (34) when transformed into a first order system, assume the form described by Eq. (39), where

$$A = \begin{pmatrix} 0_{n\times n} & I_{n\times n} \\ -\left(M_e^{-1}K_e\right)_{n\times n} & -\left(M_e^{-1}C_e\right)_{n\times n} \end{pmatrix}, \quad B = \begin{pmatrix} 0_{n\times m} \\ \left(B_e\right)_{n\times m} \end{pmatrix}, \quad x(t) = \begin{Bmatrix} \delta q(t) \\ \delta \dot{q}(t) \end{Bmatrix}.$$

For the analysis presented in subsequent sections, the perturbed air-breathing hypersonic vehicle dynamics are represented by a linearized system consisting of 12 rigid body modes, with six displacements and six velocities describing motion in a six degree of freedom space, and 28 flexible modes, where 14 of them represent vibrational displacement, while the other 14 represent vibrational velocities.

VI. Open-loop Stability Analysis

Equation (34) governs the behavior of the system under the influence of perturbed initial conditions that are small in magnitude. The linearized system is modeled by taking into account longitudinal, lateral, and directional dynamics coupled with transverse and lateral bending, transverse and lateral shear, and torsion. Neglecting higher order flexible modes, which usually get damped out rapidly during motion, results in a system that has a dimension of 40. Further, five control inputs are used to compensate for deviations from the equilibrium during cruise, given by the normalized fuel equivalence ratio, two elevon deflections, and two rudder deflections. Figure 9 presents a comparison between the open-loop eigenvalues from Bolender-Doman model and the proposed model. It can be seen that the inclusion of higher free vibration modes has resulted in several lightly damped/weakly unstable high frequency eigenmodes, which were neglected in the modeling efforts made so far. The existence of such modes presents a control problem that is much more challenging than the ones tackled in the literature.

Table 2 presents a comparison between the first 12 free vibration frequencies and eigenfrequencies of the aeroelastic system. Due to the separation between the eigenfrequencies of the first 12 eigenmodes and the remaning 28 modes, it can be concluded that the first 12 modes represent motion dominated by transport variables

$$\left\{p_{v_1},\, p_{v_2},\, p_{v_3},\, \theta_{VI_1},\, \theta_{VI_2},\, \theta_{VI_3},\, \dot{p}_{v_1},\, \dot{p}_{v_2},\, \dot{p}_{v_3},\, \dot{\theta}_{VI_1},\, \dot{\theta}_{VI_2},\, \dot{\theta}_{VI_3}\right\}^T.$$

Further, modal analysis is carried out on the linear time-invariant system Eq.(39).

Early efforts in estimating the relative contribution of a given mode on a particular state in linear time-invariant systems (LTI) date back to the early 1980s, where van Ness et al. [45] and Verghese et al. [46] carried out modal analysis to estimate the extent of impact unstable modes have on state variables of systems that model the dynamics of large scale complex power system networks. The method implemented by van Ness et al. [45] utilizes the relative element magnitudes of the right eigenvector associated with a certain mode to estimate the relative impact on state variables if that particular mode were excited. The relative element magnitudes of the right eigenvector represent the peak amplitudes of various components of the state vector for a given mode. When dealing with large scale coupled systems, it is important to study the relative distribution of modal energies among state variables as the

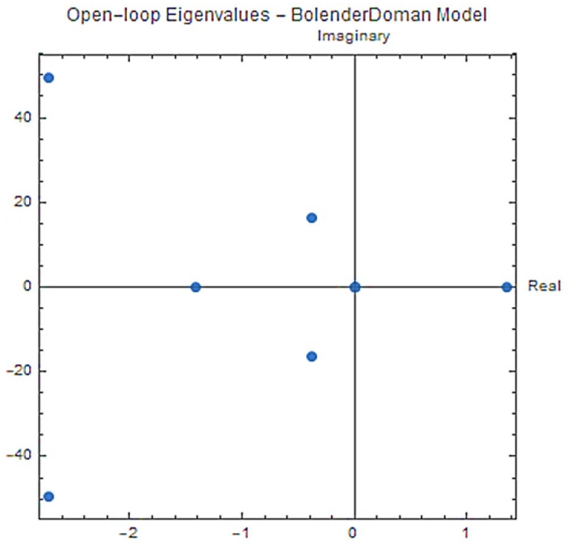

Fig. 9a)
Open-loop eigenvalues obtained from Bolender-Doman model for an air-breathing hypersonic vehicle

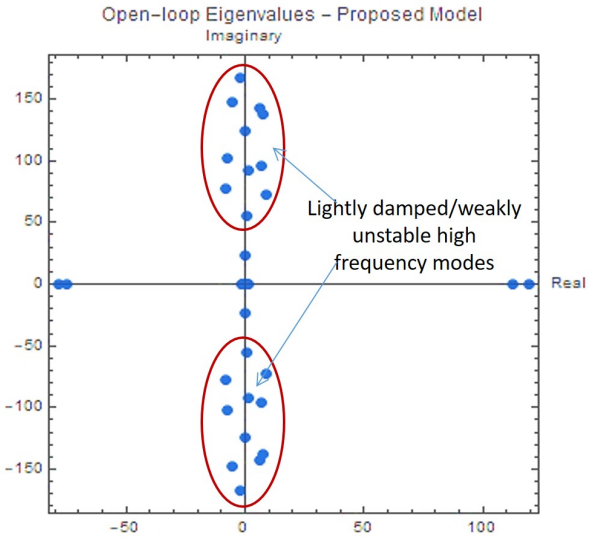

Fig. 9b)
Open-loop eigenvalues obtained from the proposed model for an air-breathing hypersonic vehicle

Figure 9: Open-loop eigenvalues in complex plane.

Table 2: Frequencies of first 12 eigenmodes.

Free vibration frequency (rad/s)	Open-loop frequency (rad/s)
0	$-2.82848 \times 10^{-7} - j0.00725462$
0	$-2.82848 \times 10^{-7} + j0.00725462$
0	$\mathbf{6.07419 \times 10^{-7} - j0.00943816}$
0	$\mathbf{6.07419 \times 10^{-7} + j0.00943816}$
0	-0.303404
0	$\mathbf{0.161859 - j0.501131}$
0	$\mathbf{0.161859 + j0.501131}$
0	$\mathbf{0.582026 - j0.298133}$
0	$\mathbf{0.582026 + j0.298133}$
0	$\mathbf{1.51106}$
0	$-1.593 - j0.0832272$
0	$-1.593 + j0.0832272$

Table 3: Axial-transverse eigenfrequencies.

Free vibration frequency (rad/s)	Open-loop frequency (rad/s)
24.68151	$-0.212027 - j23.8293$
24.68151	$-0.212027 + j23.8293$
37.810596	$\mathbf{0.915203 - j55.0409}$
37.810596	$\mathbf{0.915203 + j55.0409}$
53.711302	$\mathbf{8.56883 - j72.8971}$
53.711302	$\mathbf{8.56883 + j72.8971}$
69.504044	-74.969
69.504044	$-8.12756 - j77.192$
79.086391	$-8.12756 + j77.192$
79.086391	$\mathbf{6.9294 - j96.4822}$
93.51508	$\mathbf{6.9294 + j96.4822}$
93.51508	$-7.66357 - j102.625$
111.746287	$-7.66357 + j102.625$
111.746287	$\mathbf{119.267}$
123.390325	$\mathbf{0.323248 - j124.017}$
123.390325	$\mathbf{0.323248 + j124.017}$
135.48118	$\mathbf{7.30685 - j137.952}$
135.48118	$\mathbf{7.30685 + j137.952}$
151.72034	$-5.59096 - j147.4$
151.72034	$-5.59096 + j147.4$

Table 4: Lateral-torsional eigenfrequencies.

Free vibration frequency (rad/s)	Open-loop frequency (rad/s)
54.05765	-78.3153
54.05765	$\mathbf{1.34903 - j91.6782}$
91.47149	$\mathbf{1.34903 - +j91.6782}$
91.47149	$\mathbf{112.376}$
130.27299	$\mathbf{6.40034 - j143.048}$
130.27299	$\mathbf{6.40034 + i143.048}$
168.28852	$-2.29565 - j167.122$
168.28852	$-2.29565 + j167.122$

dynamics of such systems are driven by continuous exchange of energy between modes. The method implemented by Verghese et al. [46] extends the work of MacFarlane [47] to carry out selective modal analysis of large scale, coupled, linear time invariant systems. Let the eigenvectors for the linearized state matrix A be a basis $U = \{u_1, u_2, u_3, \ldots, u_n\}$ and the set of vectors representing the reciprocal basis be given by $V = \{v_1, v_2, v_3, \ldots, v_n\}$ such that

$$v_i^T u_j = \delta_{ij}, \qquad i, j = 1, 2, 3, \ldots, n. \tag{40}$$

The unforced (open loop) response $\mathbf{x}(t)$ of the system depends on the state variable vector, the system's transient dynamics around the equilibrium, and the initial condition $\mathbf{x}_0$,

$$\mathbf{x}(t) = \exp(A\,t)\,\mathbf{x}_0, \qquad \text{for } t \geq 0. \tag{41}$$

Assuming A is not a defective matrix, which is typical for systems representing aircraft dynamics, the fractional contribution of the jth eigenmode's response in the ith state variable at $t = 0$ is

$$w_{ij} = (v_j)_i \, (u_j)_i \,, \qquad i, j = 1, 2, 3, \ldots, n, \tag{42}$$

where $(\cdot)_i$ is the ith element of the vector $(\cdot)$. The modal participation factor matrix is formed by accumulating these element-wise products for all the eigenmodes. The percent contribution of a given state variable x_i due to the j^{th} eigenmode is

$$PMPF(i, j) = 100 \frac{|w_{ij}|}{\sum_{i=1}^{n} |w_{ij}|}. \tag{43}$$

Table 3 presents a comparison between the axial-transverse free vibration modes and aeroelastic eigenmodes dominated by axial-transverse modal coordinates. Note the jump in eigenfrequency from mode 12 to 13 between Tables 2 and 3, where the frequency goes from 0.158458 rad/s to 23.8296 rad/s marking the beginning of eigenmodes dominated by modal coordinates. The classification between eigenmodes dominated by axial-transverse modal coordinates and lateral-torsional modal coordinates is done by analyzing the PMPF matrix. Two modes of interest in this analysis are modes 29 (112.376 rad/s, classified as lateral-torsional) and 30 (119.267 rad/s, classified as axial-transverse), which are unstable, seen to the far right in Fig. 9. From the percent modal participation factor plots shown in Fig. 10 for these modes, it can be concluded that rigid body states (yaw rate $\dot{\theta}_{v_3}$ and pitch rate $\dot{\theta}_{v_2}$) dominate the participation for each of these modes. In other words, the energies associated with these two high frequency unstable modes receive an 81.5% contribution from yaw rate (mode 29, 112.376 rad/s) and a 78.2% from pitch rate (mode 30, 119.267 rad/s), respectively. When excited, these modes could be detrimental to the aircraft's stability. Further, due to such high participation from transport variables these modes can not be damped out due to material damping, and require efficient feedback control laws to achieve stability.

Mode - 30	Mode - 29
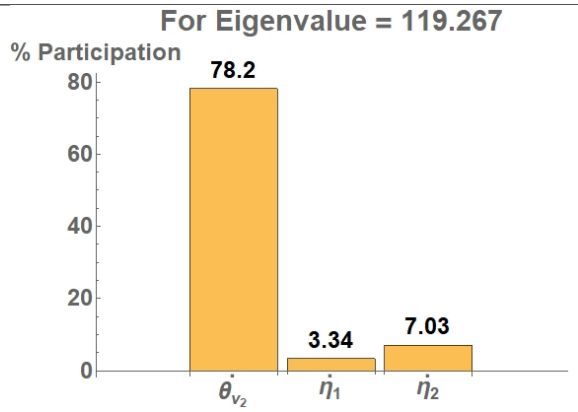	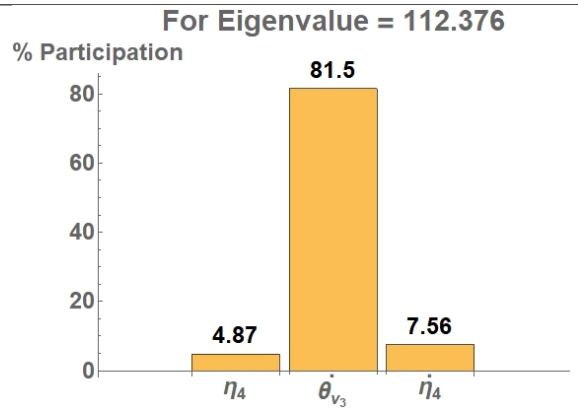
(a) The states, from left to right, are $\dot{\theta}_{v_2}$, $\dot{\eta}_1$, and $\dot{\eta}_2$.	(b) The states, from left to right, are η_4, $\dot{\theta}_{v_3}$, and $\dot{\eta}_4$.

Figure 10: PMPF bar plots for modes 30 and 29.

VII. Linear Quadratic Regulator

With the advent of multidisciplinary design optimization tools, the need for an integrated modeling and analysis environment for high speed aircraft has increased substantially over the past two decades. The ever growing increase in performance expectations has made the traditional design approach of optimize first, integrate later obsolete. Integrated design methodologies focus on optimizing the overall design, as opposed to individual subsystems. Control-oriented modeling is an approach that involves making appropriate assumptions while modeling various subsystems in order to facilitate the inclusion of control design tools during the conceptual design phase. The design framework developed so far is tailored towards obtaining optimal control laws in order to ensure that the aircraft stays on the desired trajectory. At its core, this problem involves compensating for deviation in initial conditions caused by sudden gusts. For the problem defined here, a linear quadratic regulator (LQR) is a good choice due to its reliability and ease of implementation. Just like any optimization problem, optimal control design involves minimizing an objective function that is of particular interest to the user.

In order to guarantee closed loop stability, the linearized system of equations, given by Eq. (39), must satisfy (using standard LQR notation and terminology) [48]

1. The system (A, B) must be stabilizable.
2. The state weighting matrix Q must be positive semidefinite and the control weighting matrix R must be positive definite.
3. The system (A, $\sqrt{Q}$) must be detectable.

From Fig. 9, it is evident that the open-loop system is unstable and, hence, the system requires a compensation mechanism, for example through full-state feedback. Full state feed-

back for flexible vehicles can be practically achieved via fiber optic sensing system (FOSS) that employs thousands of fiber Bragg grating (FBG) sensors integrated into a single fiber along with a combination of optical frequency domain reflectometry (OFDR) and wavelength division multiplexing (WDM) for high spatial resolution and high speed strain measurements [49]. In additon to its high temporal and spatial sampling rate, FOSS can operate at temperatures as high as 1000°C and is immune to electromagnetic interference [50]. Strain measurements are multiplexed from the sensors and fed to algorithms that estimate the shape of the aircraft [51] and loads along the fiber [52] in real-time.

In optimal control, it is important to pick an appropriate objective function that has some physical significance. Consider minimizing the objective function

$$\begin{aligned}\mathcal{J} = &\int_0^\infty p_3 p_4 \left(\frac{1}{n_h^2}(\delta x_1(t)^2 + \delta x_2(t)^2 + \delta x_3(t)^2) + \frac{1}{n_\theta^2}(\delta x_4(t)^2 + \delta x_5(t)^2 + \delta x_6(t)^2)\right) dt \\ &+ \int_0^\infty p_1 p_3 p_4 \left(\frac{1}{n_v^2}(\delta x_{n+1}(t)^2 + \delta x_{n+2}(t)^2 + \delta x_{n+3}(t)^2) + \frac{1}{n_\theta^2}(\delta x_{n+4}(t)^2 + \delta x_{n+5}(t)^2 + \delta x_{n+6}(t)^2)\right) dt \\ &+ \int_0^\infty p_4 \left(\left(\frac{\delta\phi(t)^2}{n_\phi^2}\right) + p_2 \left(\frac{\Delta\delta_{cs_1}(t)^2}{n_{\Delta_{1,2}}^2} + \frac{\Delta\delta_{cs_2}(t)^2}{n_{\Delta_{1,2}}^2} + \frac{\Delta\delta_{cs_3}(t)^2}{n_{\Delta_{3,4}}^2} + \frac{\Delta\delta_{cs_4}(t)^2}{n_{\Delta_{3,4}}^2}\right)\right) dt,\end{aligned} \tag{44}$$

where p_1, p_2, p_3, and p_4 are positive parameters. Further, the first two rows of Eq. (44) represent a normalized measure of the perturbed rigid body states, where n_h, n_θ, and n_v are expected maximum perturbations of the respective states. These constants are used for normalization purposes, hence, they are lumped based on the order of the states. Row three of Eq. (44) is a normalized measure of the control inputs. The designer has the choice to prioritize between the rigid body positions and velocities by choosing the parameter p_1 and the choice to prioritize between the fuel equivalence ratio and control surface deflections via p_2. Further, the designer has a choice to prioritize between the deviation in states (δx) and the additional control effort needed (δu) through p_3, and p_4 is a stability tuning parameter for the algebraic Riccati solver. The objective function used in optimal control design is of the form

$$\mathcal{J} = \int_0^\infty \left(\{\delta x\}^T \left[p_3\, p_4\, Q(p_1)\right] \{\delta x\} + \{\delta u\}^T \left[p_4\, R(p_2)\right] \{\delta u\}\right) dt, \tag{45}$$

where

$$Q(p_1) = \begin{pmatrix} (1/n_h^2)\,\mathbb{I}_{3\times3} & \mathbf{0}_{3\times3} & \mathbf{0}_{3\times n-6} & \mathbf{0}_{3\times3} & \mathbf{0}_{3\times3} & \mathbf{0}_{3\times n-6} \\ \mathbf{0}_{3\times3} & (1/n_\theta^2)\,\mathbb{I}_{3\times3} & \mathbf{0}_{3\times n-6} & \mathbf{0}_{3\times3} & \mathbf{0}_{3\times3} & \mathbf{0}_{3\times n-6} \\ \mathbf{0}_{n-6\times3} & \mathbf{0}_{n-6\times3} & \mathbf{0}_{n-6\times n-6} & \mathbf{0}_{n-6\times3} & \mathbf{0}_{n-6\times3} & \mathbf{0}_{n-6\times n-6} \\ \mathbf{0}_{3\times3} & \mathbf{0}_{3\times3} & \mathbf{0}_{3\times n-6} & (p_1/n_v^2)\,\mathbb{I}_{3\times3} & \mathbf{0}_{3\times3} & \mathbf{0}_{3\times n-6} \\ \mathbf{0}_{3\times3} & \mathbf{0}_{3\times3} & \mathbf{0}_{3\times n-6} & \mathbf{0}_{3\times3} & (p_1/n_\theta^2)\,\mathbb{I}_{3\times3} & \mathbf{0}_{3\times n-6} \\ \mathbf{0}_{n-6\times3} & \mathbf{0}_{n-6\times3} & \mathbf{0}_{n-6\times n-6} & \mathbf{0}_{n-6\times3} & \mathbf{0}_{n-6\times3} & \mathbf{0}_{n-6\times n-6} \end{pmatrix}, \tag{46}$$

$$\text{and} \quad R(p_2) = \begin{pmatrix} 1/n_\phi^2 & 0 & 0 & 0 & 0 \\ 0 & p_2/n_{\Delta_{1,2}}^2 & 0 & 0 & 0 \\ 0 & 0 & p_2/n_{\Delta_{1,2}}^2 & 0 & 0 \\ 0 & 0 & 0 & p_2/n_{\Delta_{3,4}}^2 & 0 \\ 0 & 0 & 0 & 0 & p_2/n_{\Delta_{3,4}}^2 \end{pmatrix}. \tag{47}$$

For the present analysis, the normalization factors were chosen to be the maximum permissible deviations from equilibrium. The values for the present case are

$$n_h = 100 \text{ m}, \qquad n_\theta = \frac{5\pi}{180} \text{ rad}, \qquad n_v = 10 \text{ m/s},$$
$$n_\phi = 1, \qquad n_{\Delta_{1,2}} = 4.5916\frac{\pi}{180} \text{ rad}, \qquad n_{\Delta_{3,4}} = 2\frac{\pi}{180} \text{ rad}.$$

The cost function, $\mathcal{J}$, is parametrized by p_1, p_2, p_3, p_4, where p_1 shifts emphasis between rigid body positions and velocities, p_2 shifts emphasis between fuel equivalence ratio and control surface deflections, p_3 shifts emphasis between the state variables and control variables, and p_4 is a stability tuning parameter for the algebraic Riccati solver.

The optimal control law for the case of full state feedback is

$$u(t) = -K\,x(t), \tag{48}$$

where

$$K = -R^{-1}B^T P. \tag{49}$$

The optimal control gain is computed by solving the matrix algebraic Riccati equation

$$PA + A^T P - PBR^{-1}B^T P + Q = 0 \tag{50}$$

for the positive definite matrix P. A parametric study was conducted, where parameters p_1, p_2, and p_3 were varied within the range 0.1 to 10. p_4, on the other hand, was tuned to a value of 10 as the algebraic Riccati solver consistently converged in that range. The effectiveness of the tuned parameter is expressed in the form of a scalar stability measure SM, which is given by the perpendicular distance between the least stable, stable mode and the imaginary axis

$$SM = \min_{i=1,\ldots,n} \left\{ \text{Re}\,(\lambda_i) \,\middle|\, \text{Re}\,(\lambda_i) < 0 \right\}, \tag{51}$$

where λ_i is the ith eigenvalue of the linearized state matrix A. In other words, a search is conducted for the parameter that yields closed-loop performance, where the least stable eigenvalue has the largest real part across the entire parameter range. Figure 11 shows that the maximum stability measure is observed at $p_3 = 0.1$. Figure 12 presents a parametric variation of weights p_1 and p_2 when $p_3 = 0.1$. The parametric analysis indicates that placing greater emphasis on deviations in positions (as opposed to velocities), and fuel equivalence ratio (as opposed to control surface deflections) result in more stable control laws, as per

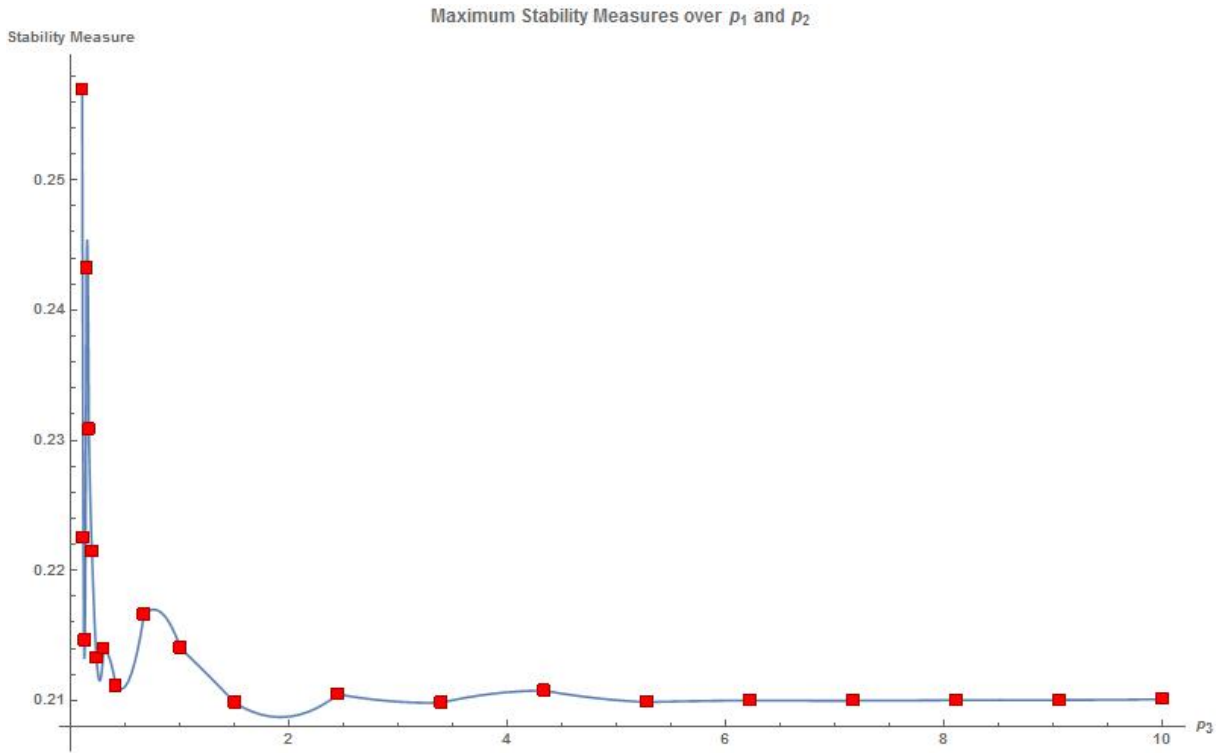

Figure 11: Parametric variation of p_3 and the maximum stability measures.

the scalar stability measure defined above. Figure 11 presents a parametric variation of p_3 indicating that placing greater emphasis on control effort (as opposed to perturbations in state) yield a higher stability measure. The best stability measure over the parameter range is observed at

$$p_1 = 0.160714, \qquad p_2 = 0.189474, \qquad p_3 = 0.1, \qquad p_4 = 10.$$

The closed loop eigenvalues for the parameters presented above are shown in Fig. 13 in comparison to the open-loop eigenvalues. It is important to note that although the closed-loop system is exponentially stable for all the parameter values, the above set of parameters give the best stability measure by moving the least stable mode(s) farther left from the imaginary axis.

VIII. Conclusions

The design of future high speed aircraft requires advanced modeling tools to make the design process affordable and reliable. Such vehicles experience extreme aerodynamic loads causing significant flexing of the airframe, which leads to deflections in the thrust vector due to an airframe tightly integrated with the propulsion system. Second order nonlinear equations of motion were derived for the flexible air-breathing hypersonic vehicle using the Lagrangian and principle of virtual work with the free vibration mode shapes and natural frequencies previously obtained. These nonlinear equations of motion were linearized about a

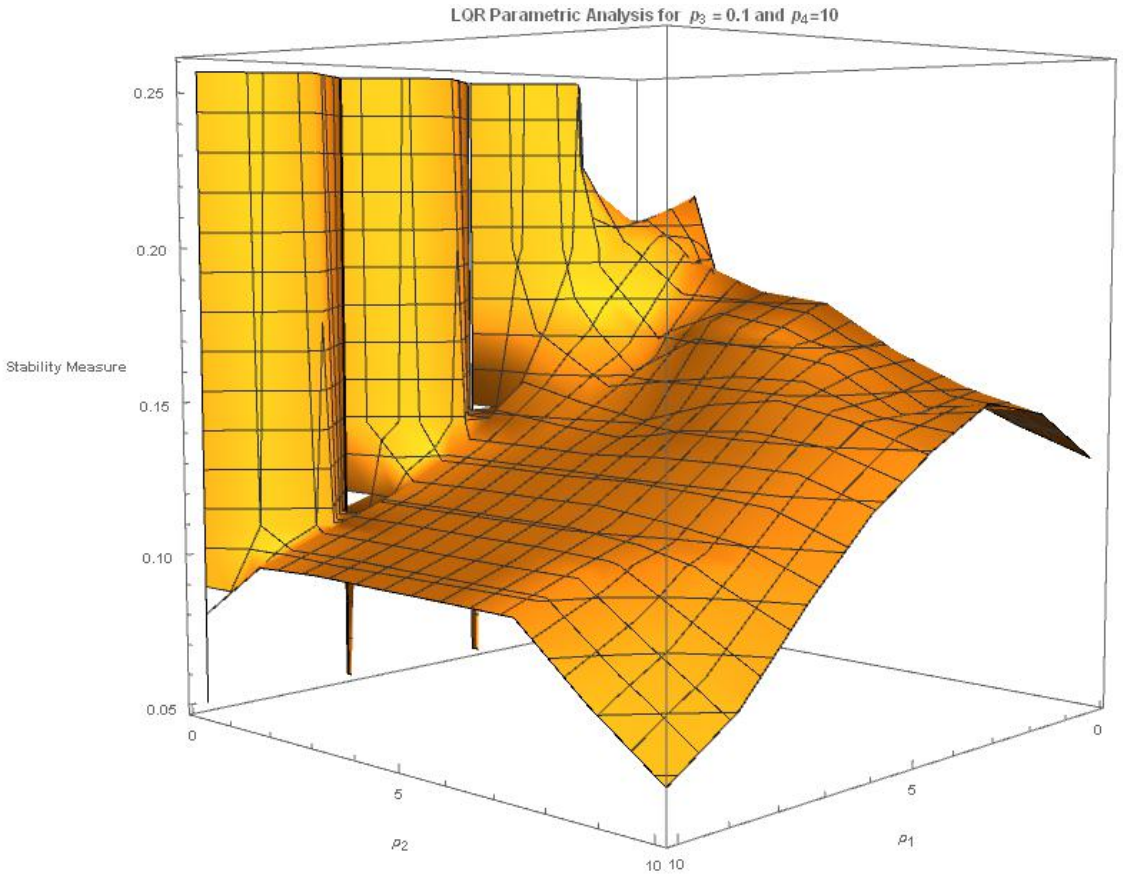

Figure 12: Stability measures for a parametric variation of p_1 and p_2, while $p_3 = 0.1$.

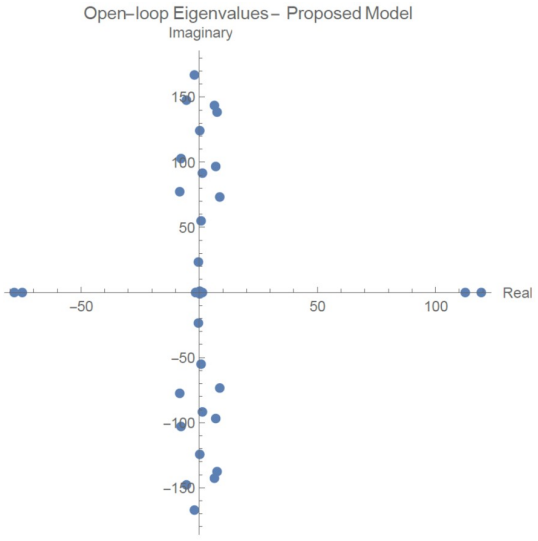

Fig. 13a)
Open-loop eigenvalues obtained from the proposed model for an air-breathing hypersonic vehicle.

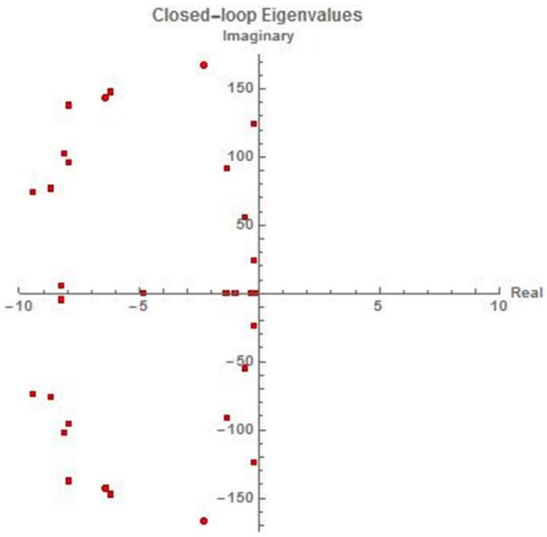

Fig. 13b)
Closed-loop eigenvalues after implementing LQR control design.

Figure 13: Closedloop eigenvalues in complex plane.

desired trajectory to obtain the linearized equations of motion, for which open-loop stability analysis was carried out. Further, a linear quadratic regulator was designed to compensate for deviations from the desired trajectory. A parametric analysis was conducted to find a set of parameters that define the most appropriate cost function (within the range of parameters chosen) to be minimized for the compensator.

Open-loop eigenvalues of the linearized system confirm the initial hypothesis that lightly damped high frequency modes arise in air-breathing hypersonic vehicle (AHV) dynamics. The proximity of high frequency modes to the imaginary axis conclusively establishes the need to include high frequency modes during the modeling phase. Modes 29 and 30 classified as unstable flexible modes with purely real eigenvalues had a considerable impact on at least one transport variable indicating a stronger coupling between modal coordinates and transport variables. Parametric variation of the cost function via p_3 reveals that a higher penalty should be placed on the control cost to obtain the highest stability margin. Further, when $p_3 = 0.1$ the parametric study showed that a higher stability margin was observed when a higher penalty was placed on positions (compared to velocities) and fuel equivalence ratio (compared to control surface deflections). The designed compensator placed closed-loop eigenvalues as far to the left as possible, for the range of parameter values considered. The algorithm DIRECT mentioned earlier could be used to set the penalties to maximize stability margin.

Acknowledgements

This material is based on fundamental research sponsored by Air Force Research Laboratory under agreement number FA8650-09-2-3938. The U.S. Government is authorized to reproduce and distribute reprints for Governmental purposes not withstanding any copyright notation thereon.

The views and conclusions contained herein are those of the authors and should not be interpreted as necessarily representing the official policies or endorsements, either expressed or implied, of Air Force Research Laboratory or the U.S. Government.

References

[1]Voland, R. T., Huebner, L. D., and McClinton, C. R., "X-43A Hypersonic Vehicle Technology Development," *Acta Astronautica*, Vol. 59, 2006, pp. 181–191, DOI: 10.1016/j.actaastro.2006.02.021.

[2]Rodriguez, A. A., Dickeson, J. J., Cifdaloz, O., McCullen, R., Benavides, J., Sridharan, S., Kelkar, A., Vogel, J. M., and Soloway, D., "Modeling and Control of Scramjet-Powered Hypersonic Vehicles: Challenges, Trends, & Tradeoffs," *AIAA Guidance, Navigation and Control Conference and Exhibit*, Honolulu, Hawaii, 2008, pp. 1–40, AIAA 2008-6793, DOI: 10.2514/6.2008-6793.

[3]Sippel, M. and Klevanski, J., "Preliminary Definition of Supersonic and Hypersonic Airliner Configuration," *14th AIAA/AHI Space Planes and Hypersonic Systems and Technology Conference*, 2006, pp. 1–17, AIAA 2006-7984, DOI: 10.2514/6.2006-7984.

[4]Klock, R. J. and Cesnik, C. E., "Aerothermoelastic Simulation of Air-breathing Hypersonic Vehicles," *55th AIAA/ASME/ASCE/AHS/ASC Structures, Structural Dynamics, and Materials Conference*, 2014, pp. 1–16, AIAA 2014-0149, DOI: 10.2514/6.2014-0149.

[5]Bolender, M. A. and Doman, D. B., "Nonlinear Longitudinal Dynamical Model of an Air-Breathing Hypersonic Vehicle," *Journal of Spacecraft and Rockets*, Vol. 44, No. 2, 2007, pp. 374–387, DOI:

10.2514/1.23370.

[6]Fiorentini, L., Serrani, A., Bolender, M. A., and Doman, D. B., "Nonlinear Control of Non-minimum Phase Hypersonic Vehicle Models," *American Control Conference 2009*, St. Louis, MO, 2009, pp. 3160–3165, DOI: 10.1109/ACC.2009.5160211.

[7]McNamara, J. J. and Friedmann, P. P., "Aeroelastic and Aerothermoelastic Analysis of Hypersonic Vehicles: Current Status and Future Trends," *48th AIAA/ASME/ASCE/AHS/ASC Structures, Structural Dynamics, and Materials Conference*, Honolulu, Hawaii, 2007, pp. 1–55, AIAA 2006-8058, DOI: 10.2514/6.2006-8058.

[8]McNamara, J. J., Culler, A. J., and Crowell, A. R., "Aerothermoelastic Modeling Considerations for Hypersonic Vehicles," *16th AIAA/DLR/DGLR International Space Planes and Hypersonic Systems and Technologies Conference*, Bremen, Germany, 2009, pp. 1–38, AIAA 2009-7397, DOI: 10.2514/6.2009-7397.

[9]Sivolella, D., *The Space Shuttle Program: A Remarkable Flying Machine*, Springer International Publishing, Cham, Switzerland, 2017, DOI: 10.1007/978-3-319-54946-0.

[10]Ward, B., *Dr. Space : The Life of Wernher von Braun*, Naval Institute Press, Annapolis, 2013, ISBN: 9781591149262.

[11]Mirmirani, M., Wu, C., Clark, A., Choi, S., and Fidan, B., "Airbreathing Hypersonic Flight Vehicle Modeling and Control, Review, Challenges, and a CFD-Based Example," *Workshop on Modeling and Control of Complex Systems*, Ayia Napa, Cyprus, June, 2005, pp. 1–15.

[12]Dolvin, D. J., "Hypersonic International Flight Research and Experimentation (HIFiRE)," *15th AIAA International Space Planes and Hypersonic Systems and Technologies Conference*, Dayton, Ohio, 2008, pp. 1–11, AIAA 2008-2581, DOI: 10.2514/6.2008-2581.

[13]Ferri, A., "Review of SCRAMJET Propulsion Technology," *Journal of Aircraft*, Vol. 5, No. 1, 1968, pp. 3–10, DOI: 10.2514/3.43899.

[14]Bertin, J. J. and Cummings, R. M., "Fifty Years of Hypersonics: Where We've Been, Where We're Going," *Progress in Aerospace Sciences*, Vol. 39, 2003, pp. 511–536, DOI: 10.1016/S0376-0421(03)00079-4.

[15]Barber, T. A., Maicke, B. A., and Majdalani, J., "Current State of High Speed Propulsion: Gaps, Obstacles, and Technological Challenges in Hypersonic Applications," *45th AIAA/ASME/SAE/ASEE Joint Propulsion Conference & Exhibit*, Denver, Colorado, 2009, pp. 1–28, AIAA 2009-5118, DOI: 10.2514/6.2009-5118.

[16]Cockrell, C. E., Auslender, A. H., Guy, R. W., McClinton, C. R., and Welch, S. S., "Technology Roadmap for Dual-mode Scramjet Propulsion to Support Space-Access Vision Vehicle Development," *AIAA/AAAF 11th International Space Planes and Hypersonic Systems and Technology*, Orleans, France, October, 2002, pp. 1–15, AIAA 2002-5188, DOI: 10.2514/6.2002-5188.

[17]Heeg, J., Zeiler, T. A., Potozky, A. S., Spain, C. V., and Engelund, W. C., "Aerothermoelastic Analysis of a NASP Demonstrator Model," Tech. rep., NASA Langley Research Center, Hampton, VA, October, 1993, NASA-TM-109007.

[18]Whitehead, A. H., "NASP Aerodynamics," *AIAA First National Aero-Space Plane Conference*, Dayton, Ohio, July, 1989, pp. 1–11, AIAA 1989-5013, DOI: 10.2514/6.1989-5013.

[19]Chavez, F. R. and Schmidt, D. K., "Analytical Aeropropulsive/Aeroelastic Hypersonic-Vehicle Model with Dynamic Analysis," *Journal of Guidance, Control, and Dynamics*, Vol. 17, No. 6, 1994, pp. 1308–1319, DOI: 10.2514/3.21349.

[20]Rausch, V. L., McClinton, C. R., and Crawford, L. J., "Hyper-x: Flight Validation of Hypersonic Airbreathing Technology," Tech. rep., NASA Langley Research Center, Hampton, VA, January, 1997, 20040110669.

[21]McClinton, C. R., Rausch, V. L., Shaw, R. J., Mehta, U., and Naftel, C., "Hyper-X: Foundation for Future Hypersonic Launch Vehicles," *Acta Astronautica*, Vol. 57, 2005, pp. 614–622, DOI: 10.1016/j.actaastro.2005.03.061.

[22]Culler, A. J., Williams, T., and Bolender, M. A., "Aerothermal modeling and Dynamic Analysis of a Hypersonic Vehicle," *AIAA Atmospheric Flight Mechanics Conference and Exhibit*, Hilton Head, South Carolina, 2007, pp. 1–21, AIAA 2007-6395, DOI: 10.2514/6.2007-6395.

[23]Chao, Y., Shu, L. G., and Qiang, W. Z., "Aerothermal-aeroelastic Two-way Coupling Method for

Hypersonic Curved Panel Flutter," *Sci China Tech Sci*, Vol. 55, 2012, pp. 831–840, DOI: 10.1007/s11431-011-4722-4.

[24]Abbas, L. K., Rui, X., Marzocca, P., Abdalla, M., and Breuker, R. D., "Non-linear Aero-Thermo-Visco-Elastic Behaviour of Geometricaly Imperfect Curved Skin Panel: Flutter and Post Flutter Analysis," *50th AIAA/ASME/ASCE/AHS/ASC Structures, Structural Dynamics, and Materials Conference*, Palm Springs, California, 2009, pp. 1–17, AIAA 2009-2596, DOI: 10.2514/6.2009-2596.

[25]Falkiewicz, N. J., Cesnik, C. E. S., Bolender, M. A., and Doman, D. B., "Thermoelastic Formulation of a Hypersonic Vehicle Control Surface for Control-Oriented Simulation," *AIAA Guidance, Navigation, and Control Conference*, Chicago, Illinois, 2009, pp. 1–18, AIAA 2009-6284, DOI: 10.2514/6.2009-6284.

[26]Bolender, M. A., "An Overview on Dynamics and Controls Modeling of Hypersonic Vehicles," *2009 American Control Conference*, St. Louis, MO, 2009, pp. 1–6.

[27]Torrez, S. M., Driscoll, J. F., Bolender, M. A., Oppenheimer, M. W., and Doman, D. B., "Effects of Improved Propulsion Modeling on the Flight Dynamics of Hypersonic Vehicles," *AIAA Atmospheric Flight Mechanics Conference and Exhibit*, Honolulu, Hawaii, 2008, pp. 1–22, AIAA 2008-6386, DOI: 10.2514/6.2008-6386.

[28]Vick, T. J., Muse, J. A., and Bolender, M. A., "Hypersonic Vehicle Model Generator for MASIV," *AIAA Modeling and Simulation Technologies Conference*, Minneapolis, Minnesota, 2012, pp. 1–38, AIAA 2012-4563, DOI: 10.2514/6.2012-4563.

[29]Falkiewicz, N. J. and Cesnik, C. E. S., "A Reduced-Order Modeling Framework for Integrated Thermo-Elastic Analysis of Hypersonic Vehicles," *50th AIAA/ASME/ASCE/AHS/ASC Structures, Structural Dynamics, and Materials Conference*, Palm Springs, California, 2009, pp. 1–18, AIAA 2009-2308, DOI: 10.2514/6.2009-2308.

[30]Vogel, J. M., Kelkar, A. G., Inger, G., Whitmer, C., Sidlinger, A., and Rodriguez, A., "Control-Relevant Modeling of Hypersonic Vehicles," *2009 American Control Conference*, St. Louis, MO, 2009, pp. 1–6, DOI: 10.1109/ACC.2009.5160682.

[31]Colgren, R., Keshmiri, S., and Mirmirani, M., "Nonlinear Ten-Degree-of-Freedom Dynamics Model of a Generic Hypersonic Vehicle," *Journal of Aircraft*, Vol. 46, No. 3, 2009, pp. 800–813, DOI: 10.2514/1.35644.

[32]Keshmiri, S., "Nonlinear and Linear Longitudinal and Lateral-Directional Dynamical Model of Air-breathing Hypersonic Vehicle," *15th AIAA International Space Planes and Hypersonic Systems and Technologies Conference*, Dayton, Ohio, 2008, pp. 1–24, AIAA 2008-2531, DOI: 10.2514/6.2008-2531.

[33]Fiorentini, L., Serrani, A., Bolender, M. A., and Doman, D. B., "Nonlinear Control of a Hypersonic Vehicle with Structural Flexibility," *47th IEEE Conference on Decision and Control*, Cancun, Mexico, 2008, pp. 578–583, DOI: 10.1109/CDC.2008.4739001.

[34]Fiorentini, L., Serrani, A., Bolender, M. A., and Doman, D. B., "Robust Nonlinear Sequential Loop Closure Control Design for an Air-breathing Hypersonic Vehicle Model," *American Control Conference 2008*, Seattle, Washington, 2008, pp. 3458–3463, DOI: 10.1109/ACC.2008.4587028.

[35]Sigthorsson, D. O., Jankocsky, P., Serrani, A., Yurkovich, S., Bolender, M. A., and Doman, D. B., "Robust Linear Output Feedback Control of an Air-breathing Hypersonic Vehicle," Vol. 31, 2008, pp. 1052–1066, DOI: 10.2514/1.3230.

[36]Sigthorsson, D. O., Serrani, A., Bolender, M. A., and Doman, D. B., "LPV Control Design for Over-actuated Hypersonic Vehicles Models," *AIAA Guidance, Navigation, and Control Conference*, Chicago, Illinois, 2009, pp. 1–24, AIAA 2009-6280, DOI: 10.2514/6.2009-6280.

[37]Parker, J. T., Serrani, A., Yurkovich, S., Bolender, M., and Doman, D. B., "Control-oriented Modeling of an Air-breathing Hypersonic Vehicle," *Journal of Guidance, Control, and Dynamics*, Vol. 30, No. 3, 2007, pp. 856–869, DOI: 10.2514/1.27830.

[38]Sudalagunta, P. R., Sultan, C., Kapania, R. K., Watson, L. T., and Raj, P., "Accurate Computing of Higher Vibration Modes of Thin Flexible Structures," *AIAA Journal*, Vol. 54, No. 5, 2016, pp. 1704–1718, DOI: 10.2514/1.J054428.

[39]Sudalagunta, P. R., Sultan, C., Kapania, R. K., Watson, L. T., and Raj, P., "A Novel Scheme to Accurately Compute Higher Vibration Modes using the Ritz Method and a Two-point BVP Solver," *56th AIAA/ASCE/AHS/ASC Structures, Structural Dynamics, and Materials Conference*, Kissimmee, Florida, 2015, pp. 1–18, AIAA 2015-1166, DOI: 10.2514/6.2015-1166.

[40]Sudalagunta, P. R., Sultan, C., Kapania, R. K., Watson, L. T., and Raj, P., "Aeroelastic Control-oriented Modeling of an Air-breathing Hypersonic Vehicle," *15th Dynamics Specialists Conference*, San Diego, California, 2016, pp. 1–25, AIAA 2016-1325, DOI: 10.2514/6.2016-1325.

[41]Ward, D. T. and Stragnac, T. W., *Introduction to Flight Test Engineering*, Kendall Hunt Publishing, Iowa, 2006.

[42]Sudalagunta, P. R., *Control-oriented Modeling of an Air-breathing Hypersonic Vehicle*, Ph.D. thesis, Virginia Polytechnic Institute and State University, Blacksburg, VA, 2016.

[43]Jones, D. R., Perttunen, C. D., and and, B. E. S., "Lipschitzian Optimization Without the Lipschitz Constant," *Journal of Optimization Theory and Application*, Vol. 79, No. 1, 1993, pp. 157–181, DOI: 10.1007/BF00941892.

[44]Smith, L. B., "Measurement of Winds between 100, 000 and 300, 000 ft by use of Chaff Rockets," *Journal of Meteorology*, Vol. 17, 1960, pp. 296–310, DOI: 10.1175/1520-0469(1960)017¡0296:TMOWBA¿2.0.CO;2.

[45]Ness, J. . E. V., Brasch, F. M., Landgren, G. L., and Naumann, S. T., "Analytical Investigation of Dynamic Instability Occuring at Powerton Station," *IEEE Transactions on Power Apparatus and Systems*, , No. 4, 1980, pp. 1386–1395, DOI: 10.1109/TPAS.1980.319561.

[46]Varghese, G. C., Perez-Arriaga, I. C., and Schweppe, F. C., "Selective Modal Analysis with Applications to Electric Power Systems, Part I: Heuristic Introduction," *IEEE Transactions on Power Apparatus and Systems*, , No. 9, 1982, pp. 3117–3125, DOI: 10.1109/TPAS.1982.317525.

[47]MacFarlane, A. G. J., "Use of Power and Energy Concepts in the Analysis of Multivariable Feedback Controllers," *Proceedings of the Institution of Electrical Engineers*, Vol. 116, No. 8, 1969, pp. 1449–1452, DOI: 10.1049/piee.1969.0261.

[48]Stengel, R. F., *Optimal Control and Estimation*, Dover Publications, New York, 1994.

[49]Parker, A. R., Chan, H. M., Richards, W. L., Piazza, A., and Hamory, P. J., "High Speed and High Spatial Density Parameter Measurement using Fiber Optic Sensing Technology," February 2017, US Patent 9,664,506; IPC G01B 11/16 G02B 6/293 G02B 6/02.

[50]Mihailov, S. J., "Fiber Bragg Grating Sensors for Harsh Environments," *Sensors*, Vol. 12, 2012, pp. 1898–1918, DOI: 10.3390/s120201898.

[51]Ko, W. L. and Richards, W. L., "Method for Real-time Structure Shape Sensing," April 2009, US Patent 7,520,176; IPC G01N 3/00 G01L 1/24.

[52]Parker, A. R., Chan, H. M., Richards, W. L., Piazza, A., and Hamory, P. J., "High Speed and High Spatial Density Parameter Measurement using Fiber Optic Sensing Technology," May 2010, US Patent 7,715,994; IPC G01L 1/00.